Master's Thesis

Nanowires and Molecular Dyes for Artificial Light-Driven Synapses and Neurons

Xinyu He
xi4280he-s@student.lu.se

December 12, 2025

LUNDS UNIVERSITET

Division of Synchrotron Radiation Research, Department of Physics, Lund University

Supervisor: **Anders Mikkelsen**, anders.mikkelsen@sljus.lu.se
Examiner: **Francesca Curbis**, francesca.curbis@maxiv.lu.se

Abstract

The development of neuromorphic computing requires devices that can use low power consumption and highly parallel architecture to process and store information, similar to the biological nervous systems. Molecular photoswitches, especially Donor–Acceptor Stenhouse Adducts (DASAs), offer a promising platform for such applications, because they undergo reversible, light-driven structural changes and show wavelength-dependent optical responses. However, to transform their molecular behavior into functional device structures, it is necessary to have a deeper understanding of how these molecules interact with nanostructure substrates, and how their optical and electrical signals evolve under controlled illumination.

This thesis studies the properties of DASA molecules AP-048 and AP-066 on both sapphire substrates and InP nanowire arrays. First, their bleaching and recovery dynamics were examined in solution and thin films to establish baseline behavior and to evaluate how casting conditions affect optical stability. Then, mixed-dye films were studied under dual-wavelength illumination to assess whether independent channels could be defined in a single molecular layer. The results show that although the spectral overlap is relatively small, the two dyes can still maintain a distinguishable response under selective excitation, and a small spectral overlap may introduce a weak additional modulation.

When integrated with vertical InP nanowire arrays, the DASA layer exhibits enhanced signal amplitude and clear photogenic electrical signal reading. By combining green and red Write/Read pulses, four different readout channels can be distinguished. Channels directly exposed to the writing wavelength display exponential decay and recovery, which is consistent with the reversible photochemical kinetics. In contrast, the indirect channels only show very small, almost linear changes. These weak residual changes are more in line with optical scattering, moderate spectral overlap, or measured background drift. According to current data, they cannot be directly attributed to molecular transitions. The comparison highlights that the dual-dye system can tolerate the slight cross-effect inherent in broadband lighting while maintaining the independence of the functional channel.

Overall, these results demonstrate that DASA-nanowire device provides a viable platform for multi-wavelength optical memory and synaptic-like functions. The combination of fast and slow response of AP-066 and AP-048 provides a variety of time dynamics in a hybrid system, suggesting the potential for scalable photonic neuromorphic devices. Future improvements may include optimizing molecular alignment, using a narrower-band excitation source, and designing nanowire geometry to further reduce crosstalk and improve device performance.

Preface

This master's thesis was completed at the Department of Physics, Division of Synchrotron Radiation Research, Lund University, 2025. The project forms part of the broader research effort in the InsectNeuroNano program, which aims to explore neuromorphic computing inspired by the navigation mechanism of the insect Central Complex. I chose this topic because it connects molecular photoswitches, semiconductor nanowires, and optoelectronic measurements, these three fields together provide a unique platform for the study of optical memory and photoelectric response.

The experimental work was conducted mainly in Lund Nano Lab and the optical laboratories of the division. I have benefited a lot from the support of several colleagues. First of all, I would like to express my sincere gratitude to my supervisor, Professor Anders Mikkelsen, for his clear guidance, constructive feedback and continuous support throughout the project. I am also deeply thankful to the PhD students who have guided and assisted me on a daily basis, Nelia Zaiats, Thomas Kjellberg Jensen, and Abhijit Das, for their patient explanations, insightful discussions, and help with both experimental design and data analysis. I am especially grateful to David Alcer, whose practical expertise was crucial to solving many laboratory and measurement-related issues.

The materials used in this work were provided by several research groups. The DASA dyes were generously supplied by Abbey Meprathu Philip, Bo Wegge Laursen and their colleagues at the University of Copenhagen. The nanowire substrate was prepared by the group of Professor Magnus Borgström at Lund University, with additional support from PhD student Mariia Lamers. Their contributions were essential for enabling the combined experiment of dye–nanowire in this thesis.

This research was conducted within the framework of the InsectNeuroNano project, part of the Horizon Europe program (GA 101046790). The project involves close collaboration between Lund University, the University of Copenhagen, the University of Edinburgh, the University of Groningen, and the International Iberian Nanotechnology Laboratory (INL). The collaborators contributed their expertise in nanowire synthesis, optical design, communication studies, and computational architecture. Regular meetings and cross-institutional cooperation have greatly enriched the scientific research environment for the completion of this thesis.

Finally, I would like to thank my family and friends for their support during this work. Their encouragement is the motivation for me to finish this thesis.

Popular science summary

Before discussing this research, it helps to look at a familiar phenomenon in daily life: why does your laptop's fan suddenly roar like a jet engine when you open several programs at once? It is not struggling with the tasks, but it has to shuttle data back and forth between the processor and the memory, and this movement is inherently inefficient.

Nature, however, works differently. Even a small creature like a bee can quickly judge whether a flower is worth approaching or if a place is dangerous. Its secret is that processing and memory usually occur in the same physical location. Synapses change their connection strength according to recent events, and the experience is recorded in subtle structural changes. There is no need to move information around; it naturally flows through the system.

This contrast has prompted scientists to ask: could materials also learn from biological synapses, changing their internal state after a stimulus and retaining it for some time? Light is a fascinating candidate for such systems. It is fast, does not interfere much with other signals, and can even "speak different languages" through different wavelengths and polarization.

Photoreversible molecules such as DASA undergo reversible structural changes under light and slowly return to their original state once the light is removed. This "bleach-and-recovery" behavior resembles a short-term memory. Earlier studies on light-responsive synapses often began with single-molecule systems. This research expands on that basis: if two molecules sensitive to different spectral regions are mixed in the same thin film, will two independent optical memory traces appear? Can the material "understand" multiple light inputs at the same time?

To explore this, we chose two types of molecules with different "personalities", each preferring a different spectral region. After mixing them, we deposited the film on a semiconductor nanowire array. This "forest of nanowire light catchers" enhances the local optical field, amplifies small molecular changes, and converts them into electrical signals so we can read the traces left by light.

When the film is illuminated with different spectral components, different molecular groups are activated, leaving their own optical memories. Although the two responses show some mutual influence, they remain distinguishable within the same material. In other words, a single device now has two different input channels. It is also observed that the polarization of the light affects the response. Light has not only "color" but also "direction", and if the material can sense this difference, future devices may encode information through both wavelength and polarization.

Although this is still an early prototype, it shows the potential of light-driven synapses in future brain-like computing. As data volumes grow and energy becomes a bottleneck, if materials can perform both "computation + memory" internally, it will help reduce energy consumption and pave the way for new computing architectures.

Table of Contents

Chapter 1 – Introduction

1.1 Background and Motivation

With the rapid development of artificial intelligence and data-driven technology, the ability to quickly process a large amount of information is becoming increasingly important. This situation puts forward higher requirements for computer hardware and overall system performance. However, most computer systems today still rely on the von Neumann architecture, in which memory and processing power are physically separated. Since the data must be repeatedly transmitted between these two units, the system will encounter the so-called von Neumann bottleneck. This continuous data transmission will increase latency and energy consumption, and has become a limiting factor for applications such as big data analysis and the Internet of Things (IoT) [1][2]. As this "memory wall" becomes more and more obvious, it is difficult for traditional architecture to meet the needs of fast and complex computing.

The biological system presents a completely different scene. The human brain can process information in parallel and consume very little energy at the same time. It can efficiently perform tasks such as voice understanding, image recognition, memory and decision-making[3]. The difference between the two systems is shown in **Figure 1.1**. The von Neumann architecture mainly works in a sequential way (**Fig. 1.1a**), while biological neural networks rely on many interconnected neurons and synapses to process information in parallel (**Fig. 1.1b**).

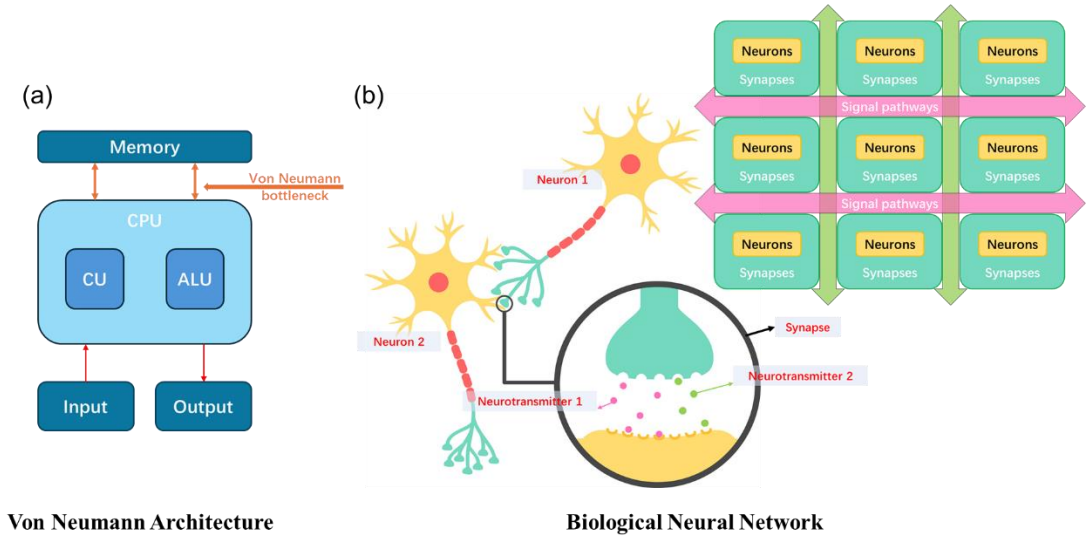

Figure 1.1. *Comparison of the von Neumann architecture (a) with the biological neural network (b).*

Neurons are the basic units of the brain and play a key role in transmitting and processing information. Synapses connect neurons with each other, and their most important feature is synaptic plasticity. This plasticity, which enables synaptic weights to be modified, is the basis of learning in the brain[4][5][6]. The human brain contains roughly 10^{11} neurons and around 10^{15} synapses, forming a very large and highly connected network. The brain achieves excellent energy efficiency through the collaboration between neurons and synapses, and its operating power consumption is only about 20 W[7]. However, the scale and complexity of the system make it extremely difficult to

reproduce directly in the artificial hardware.

What is striking is that high efficiency is not unique to human beings. Many insects also show amazing cognitive abilities. In the 19th century, Charles Darwin once described the ant's brain as "one of the most wonderful atoms of matter in the world," implying that its complexity was comparable to that of the human brain. Although the number of neurons in the brains of insects is far less than that of humans (for example, the fruit fly has about 100,000 neurons), they are still able to learn, adapt to navigate the environment[8][9]. Because their neural systems are smaller and easier to analyze, they provide valuable models for understanding how compact networks perform complex functions.

A well-known example is the desert ants, which can return to their nests very accurately even in environment that lacks obvious landmarks. It calculates the path integral by counting steps and sensing the polarization mode of sunlight, thus estimating the direction and distance (**Fig. 2A–B**)[10]. These ants also use panoramic visual scenes and local landmarks to fine-tune their routes and show flexible navigation behavior. Honeybees (Apis mellifera) demonstrate similar abilities. In the process of foraging and returning to the nest, they memorize the visual characteristics in the landscape and rely on the position of the sun and polarized light as guiding cues (**Fig. 2C**). They also communicate the location of food sources through the well-known waggle dance, thus sharing within the colony (**Fig. 2D**)[11]. Research has shown that the central complex (CX) in the insect brain is a conservative structure that integrates sensory and motor information and computes the so-called "home vector" [12]. This mechanism helps to explain how insects navigate in complex environments and how relatively small neural circuits perform advanced tasks with minimal energy.

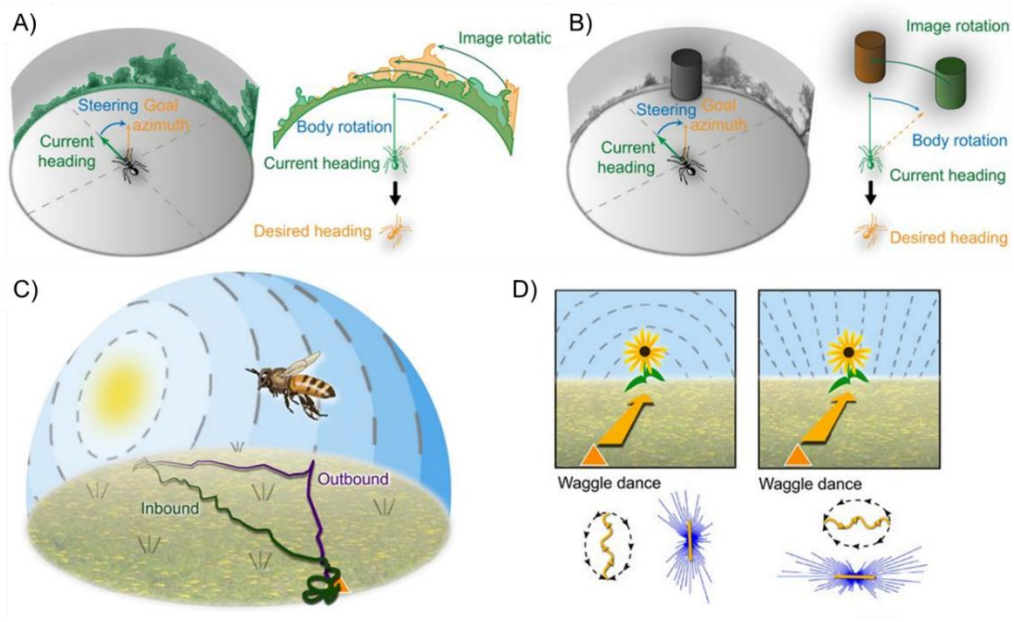

Figure 1.2. *Examples of insect navigation strategies. A) Desert ants use path integration to calculate the home vector and return to their nest[13][14]. B) In addition, desert ants rely on panoramic image matching and landmarks to correct their direction, which allows robust navigation even in complex environments[15]. C) Honeybees learn visual features and use the sun and polarized light during foraging[16]. D) Honeybees use the waggle dance to share direction and distance of food sources[17]. (Adapted from Honkanen et al.[18]).*

Inspired by these biological systems, researchers have proposed the concept of neuromorphic computing. The idea is to reproduce some of the principles of biological processing in artificial systems and to go beyond the von Neumann framework. Many electronic approaches have been explored for artificial synapses, such as memristors, CMOS-based analog or hybrid circuits, and phase-change memories. These devices have made important progress in reproducing different forms of synaptic plasticity. Even so, they still face some practical limitations in terms of scalability, energy consumption, switching speed and long-term reliability[9]. For instance, memristors often show variations between devices, nonlinear conductance changes and limited durability. CMOS circuits have difficulty achieving both high density and low power consumption at the same time. Phase-change memories are affected by heating, temperature-dependent drift, and restricted cycling lifetime, which makes fast and reversible operation challenging[19][20][21].

Optical methods, in comparison, provide unique advantages. Light travels extremely fast, supports natural parallelism, and can be separated into multiple channels by using properties such as wavelength or polarization. Channel interference can occur, but is often sufficiently small to be considered negligible in many optical systems[22][23]. For these reasons, photonics is considered one of the most promising directions for neuromorphic computing and has pointed researchers toward nanomaterials and molecular photoswitches.

1.2 State of the Art

In the research field of neuromorphic computing, photonics has attracted great attention because of its speed, natural parallelism, and low interference[24]. Among the different photonic approaches, semiconductor nanowires have gradually become core materials. In particular, III–V semiconductor nanowires show high absorption coefficients and excellent photoelectric conversion. Their one-dimensional structure also offers unique advantages for on-chip integration[22]. Recent studies have even demonstrated direct optical communication between nanowires on a chip. A single emitter–receiver pair was able to transfer information with remarkable stability and with energy use as low as the femtojoule range, which is close to or even better than the efficiency of biological synapses[25]. This indicates that nanowires can function not only as detectors or emitters but also as artificial “neurons” in neuromorphic networks.

Still, nanowires alone are not enough to create real “learning” and “memory.” In biological synapses, the dynamic regulation of synaptic weights is the key to learning. To achieve similar behavior in the artificial system, additional adjustable components are also required. Molecular photoswitches offer a promising way, as these molecules can reversibly change their structure when exposed to light and their absorption spectrum will change significantly. This realizes dynamic optical control[26][27][28]. In various photoswitch families, Donor–Acceptor Stenhouse Adducts (DASAs) have received particular attention. DASAs can be switched using visible light, showing strong and easy-to-detect color changes, and the recovery time varies from a few seconds to several hours. These properties resemble different time scales in biological memory, from short-term to long-term storage.

A recent study (**Fig. 1.3**) combined DASA molecules with nanowire optoelectronic devices to build artificial photonic synapses[29]. In this system, the DASA molecules acted as adjustable synaptic

weights. When exposed to repeated light pulses, the molecules gradually underwent photobleaching, which reduced their absorption and consequently increased the optical transmission. This strengthened the response of the next node. Once the light was removed, the molecules slowly recovered, and the device showed a kind of "forgetting" behavior. Together, these processes mimic both potentiation and depression in biological synapses.

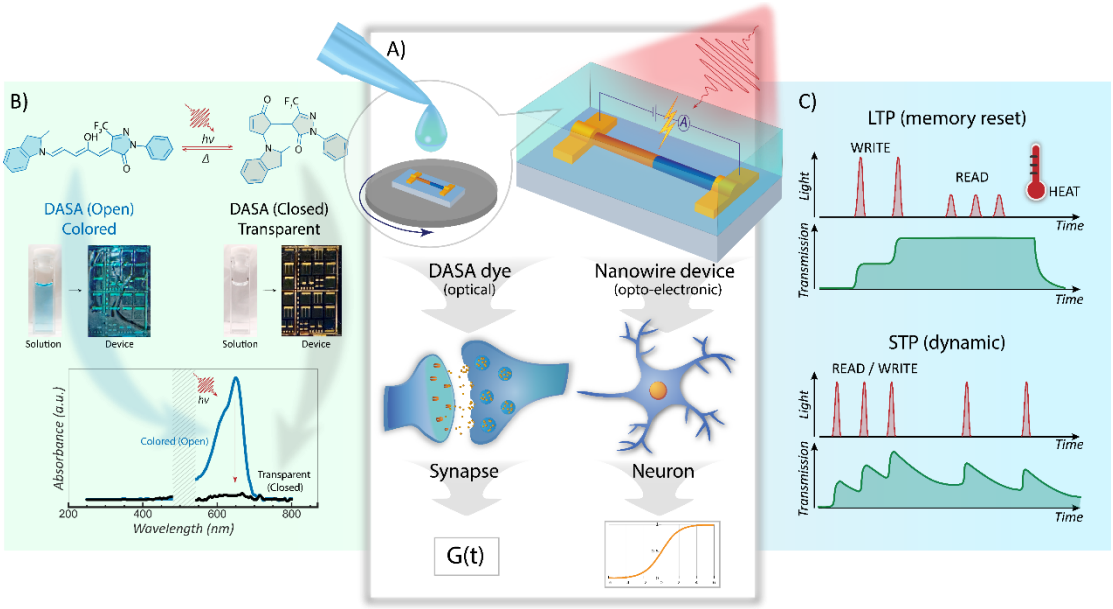

Figure 1.3. *Schematic of DASA–nanowire photonic synapse. A) Integration of DASA molecules with nanowires. B) Reversible photoisomerization of DASAs and their spectral response. C) Short-term and long-term plasticity shown in the device. Reproduced from Alcer et al., Communications Materials, 2025*[29].

The optical communication between nanowires[25] and the synaptic function of molecular photoswitches[29] complement each other: nanowires act as efficient artificial "neurons," whereas the photoswitches provide tunable "synapses". For the first time, this creates a small but clear image of an all-optical neuromorphic network.

Of course, there are still limitations. Current photonic synapse studies mostly rely on single-wavelength excitation. While this demonstrates the memory effect, it does not capture the parallel responses of biological synapses to multiple neurotransmitters. Spectral overlap between different molecules can also introduce crosstalk, which limits selectivity[30]. Stability and durability remain serious concerns, since molecules may fatigue after repeated switching and nanowires can suffer from surface and interface effects over time.

Other research directions are also being explored. **Figure 1.4** presents some examples. Low-power artificial synapses based on single GaN nanowires have been demonstrated[31]. Heterostructures of (Al,Ga)N nanowires with graphene showed synaptic behavior under interface field control[32]. BP/CdS heterostructures exhibited ultralow energy use and high sensitivity[33]. In the field of organic and flexible devices, stretchable optoelectronic synapses covered a wide spectrum from UV to near-infrared[34]. Reviews of organic photonic synapses have summarized their advantages in flexibility, integration, and biocompatibility[35]. There are also transparent ZnO nanowire synapses combining

piezoelectric and photonic effects, which provide an additional control option[36].

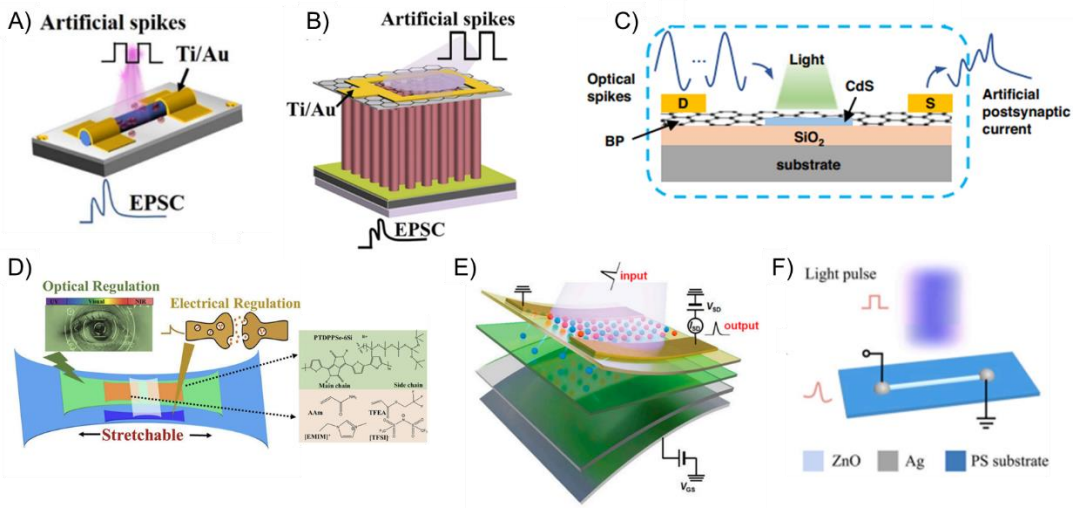

Figure 1.4. *Representative structures and working principles of various optoelectronic synaptic devices. A) Low-power synapse based on a single GaN nanowire[31]. B) Photonic synapse based on (Al,Ga)N nanowire/graphene heterojunction[32]. C) BP/CdS heterostructure with ultralow power use[33]. D) Stretchable organic photonic synapse covering UV–NIR spectrum[34]. E) Structure and mechanism of organic photonic synapse[35]. F) Transparent and flexible ZnO nanowire synapse with piezo-phototronic effect[36].*

Together these works show that optical synapses have moved from "proof of concept" to "parallel mechanisms." Still, most systems are limited by single channels, weak stability, and restricted multimodal control. For this reason, this thesis chooses to study a hybrid DASA–nanowire system. The aim is to use the reversible optical response of DASA molecules together with the efficient photoelectric conversion of nanowires to explore multi-wavelength, multi-channel, and polarization control, with the hope of getting closer to the complexity of biological synapses.

1.3 Objectives of This Thesis

Most current optical synapse studies rely on single-wavelength excitation to tune synaptic weights. This confirms the possibility of optically controlled synapses, yet it clearly limits both function and flexibility. Biological synapses, in contrast, can respond to different neurotransmitters and can also switch flexibly between short-term memory (STM) and long-term memory (LTM). This allows the brain to perform massive parallel computing with very little energy. Inspired by this, the present work proposes a multi-wavelength optical strategy. By combining it with the anisotropic optical response of nanowires, the aim is to move beyond single-channel control toward multi-dimensional artificial optical synapses.

The main objectives are as follows:

First, to study channel independence. DASA derivatives AP-048 and AP-066 have main absorption peaks at 652 nm and 568 nm. If selective excitation can be achieved so that each wavelength only affects its own molecule, it becomes possible to build independent optical channels within the same

device. In practice, however, absorption curves overlap and stray light in the system makes fully independent response difficult. Even so, testing the degree of channel independence is important, since it determines whether there is a clear mapping between input and output.

Second, to examine crosstalk and coupling. Independence and crosstalk are closely related. If one wavelength also affects another channel, a form of “crossed-line” response can appear. Such influence may arise from partial spectral overlap, energy transfer between molecules, or local environmental changes along the nanowires. Evaluating this crosstalk is important not only for understanding how independent the channels truly are, but also for deciding whether the system is more suitable for multi-channel communication or for storing mixed optical signals.

A third goal of the study is to examine the role of polarization. The DASA–nanowire structure is anisotropic, meaning that the absorption and the resulting carrier dynamics depend strongly on the polarization of the incoming light.

Finally, to evaluate stability and robustness. For any artificial synapse, stability under repeated cycles is the first condition for practical use. DASA molecules may suffer from irreversible bleaching under repeated light exposure, leading to degraded performance. This thesis therefore analyzes bleaching ratio, recovery efficiency, and timescales during repeated writing and recovery, in order to see whether the system behaves more like STM or LTM, and to assess long-term reliability.

In short, the thesis aims to answer one central question.
Can the DASA–nanowire system overcome the limits of single-wavelength control and achieve multi-wavelength and polarization-based communication, thus coming closer to the complex information processing of biological synapses?

1.4 Outline of the Thesis

The rest of the thesis is organized as follows:

Chapter 2 – Theory presents the theoretical background needed for this work. It reviews the basic physics of III–V semiconductor nanowires, including junction formation, carrier generation, and photoconductive effects. It then introduces the photophysics of DASA molecules, such as their absorption behavior, photoisomerization, and wavelength or polarization dependence. Finally, it gives a brief summary of the key ideas behind neuromorphic computing and the simple models that help describe optical modulation in dye–nanowire systems.

Chapter 3 – Methods outlines the experimental steps and measurement devices used in this project. It covers the preparation of the DASA–PAMS films, their deposition on the base of sapphire and nanowire arrays, and the optical and electrical tools applied throughout the work. The chapter also describes the illumination schemes for the Write and Read pulses, as well as data processing procedures for extracting bleaching, recovery, and synaptic signals.

Chapter 4 – Results and Discussion explains the core research findings of this thesis. First, the optical behavior of AP-048 and AP-066 was compared, focusing on their bleaching and recovery dynamics, and how different mixing ratios influence the dual-wavelength responses was examined. This chapter then studies how the DASA coated nanowire arrays respond to multi-wavelength and polarization-dependent illumination, and evaluates channel independence, crosstalk, and stability in repeated cycles. These observations are discussed in relation to the theoretical ideas introduced earlier.

Chapter 5 – Conclusion and Outlook summarizes the main conclusions of the study and their correlation with optical synapses and neuromorphic applications. It also highlights the current limitations of the system and suggests possible improvements and future directions, such as more controllable molecular alignment, improved optical interfaces, and extended device design.

Chapter 2 – Theory

2.1 Solid State Physics of III–V Nanowires

III–V compound semiconductors, such as InP and InAs, play an important role in modern optoelectronics. Their high electron mobility, direct band gaps, and strong optical absorption make them excellent materials for light–electric energy conversion at the nanoscale. This section introduces the key solid state physics underlying III–V nanowire photonic devices, including PN and PIN junction, band structures, quantum efficiency, and the interaction between light and matter in semiconductor nanowires.

2.1.1 PN and PIN Junction

(1) Intrinsic absorption and photocarrier generation

In a semiconductor, the conduction band minimum and the valence band maximum are separated by a forbidden energy gap, E_g. When a photon with energy greater than E_g is absorbed, an electron is excited from the valence band to the conduction band, leaving behind a hole. This process, called absorption, forms the basis of photoelectric conversion in semiconductor detectors (**Fig. 2.1**). The relationship between photon energy and the threshold wavelength can be written as

$$E_g = \frac{hc}{\lambda_c} \tag{1}$$

where h is Planck's constant, c is the speed of light, and λ_g is the cutoff wavelength[37]. Only photons with $\lambda < \lambda_g$ can excite electrons across the band gap. For example, InP has a band gap of about 1.34 eV, corresponding to 923 nm, which covers the visible to near-infrared range; InAs, with a smaller gap of 0.36 eV, corresponds to about 3.4 μm and is suitable for mid-infrared detection.

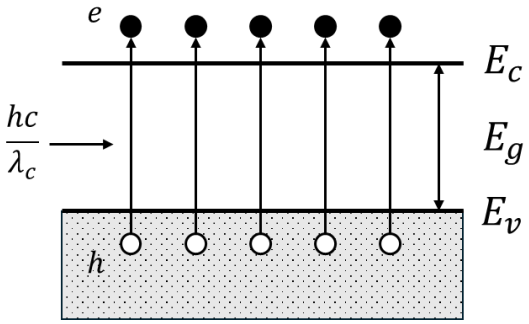

Figure 2.1. *Intrinsic absorption in a semiconductor.*

(2) Structure and operation of PN and PIN junctions

Prior to analyzing the operation of a PN junction, the formation of p-type and n-type semiconductors is briefly introduced. In an undoped semiconductor, the Fermi level (E_F) lies near the middle of the bandgap and represents the energy at which the probability of electron occupation is 50% at thermal equilibrium. Introducing acceptor dopants creates energy levels close to the valence band, producing p-type material where holes are the majority carriers. Conversely, donor doping introduces levels near the conduction band, forming n-type material dominated by electrons. Consequently, E_f shifts toward the valence band in p-type regions and toward the conduction band in n-type regions,

denoted as E_{fp} and E_{fn}, respectively, as illustrated in **Fig. 2.2(a)**. The PN junction is the fundamental element of semiconductor photodetectors[38][39]. When p-type and n-type materials contact, carriers diffuse across the interface until their Fermi levels align. This redistribution forms a built-in electric field from n to p, creating a depletion region that separates photocarriers (**Fig. 2.2**).

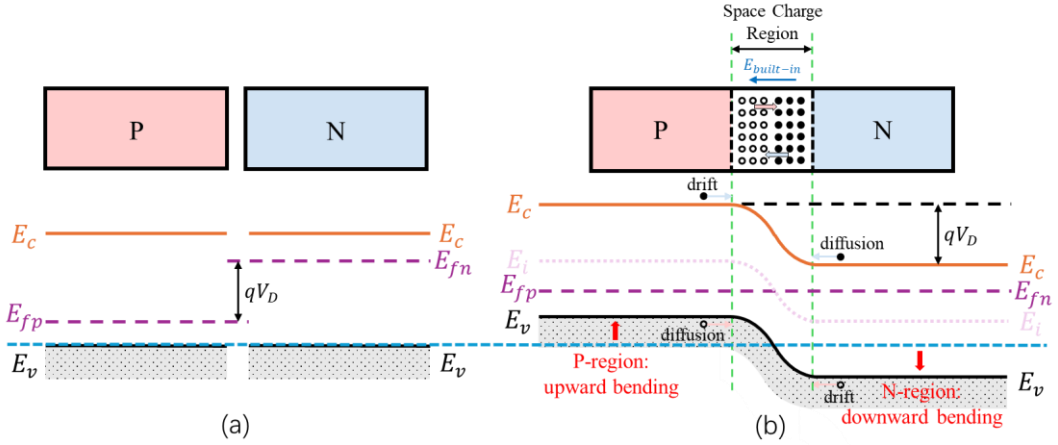

Figure 2.2. *Energy band diagrams before and after PN junction formation.* (a) Isolated p-type and n-type semiconductors. (b) PN junction at thermal equilibrium.

At equilibrium, diffusion and drift currents balance each other. When a bias is applied, band bending changes: forward bias lowers the barrier; reverse bias widens the depletion region and enhances the electric field (**Fig. 2.3**). Photodiodes usually operate under reverse bias so that photogenerated electrons move to the n side and holes to the p side, forming a photocurrent in the external circuit.

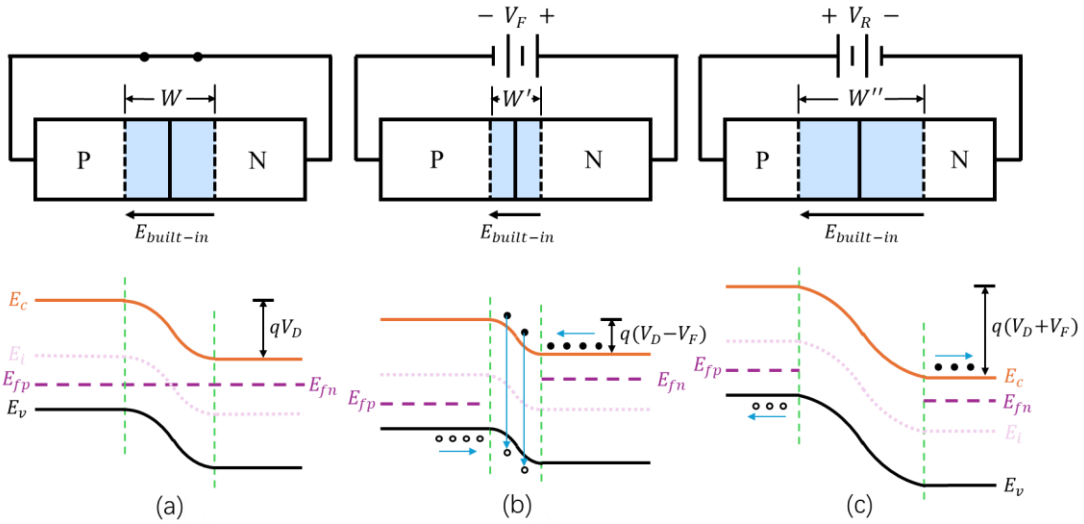

Figure 2.3. *Energy band diagrams of a PN junction under different bias conditions. (a) Zero bias; (b) Forward bias; (c) Reverse bias, showing carrier transport directions.*

Because an ordinary PN junction has a narrow depletion width, carriers generated in neutral regions must diffuse into it, which slows response and increases recombination. To improve efficiency, a lightly doped intrinsic layer (i-region) is inserted between heavily doped p and n regions, forming a PIN structure. The depletion region then extends through the entire i-layer (**Fig. 2.4**). Under reverse bias, a strong internal field (up to $10^5\ V\ cm^{-1}$) quickly separates carriers within picoseconds[40], raising quantum efficiency and temporal response[41]. The i-region also suppresses thermal carriers,

reducing dark current and improving the signal-to-noise ratio. Adjusting its thickness and bias allows a trade-off between bandwidth and sensitivity, which makes PIN structures widely adopted in photodiodes and solar cells for efficient photoelectric conversion.

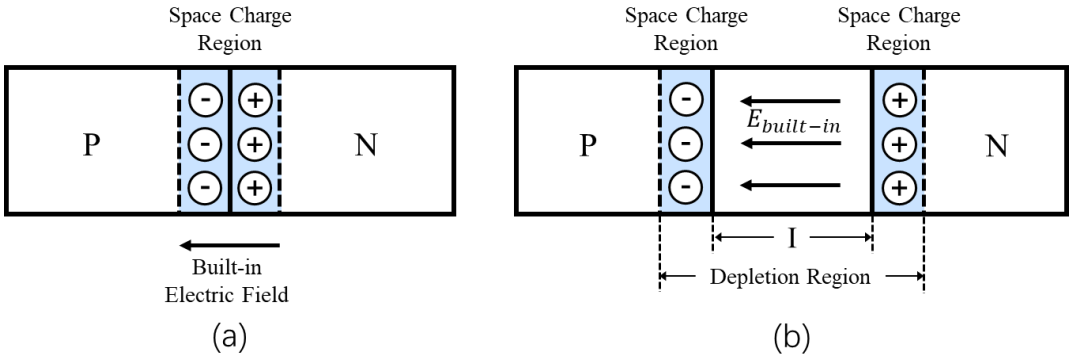

Figure 2.4. *Comparison of depletion regions in PN and PIN junctions.* (a) PN junction: narrow depletion region. (b) PIN junction: wide intrinsic region with a strong built-in field.

2.1.2 Working Principles and Material Selection (InP vs InAs)

Compared with thin films or bulk materials, nanowires exhibit enhanced absorption and carrier transport due to their one-dimensional geometric structure. Among III–V materials, InP and InAs have complementary properties and are widely used in photodetectors[42]. **Figure 2.5** shows the vertically arranged InP nanowires, forming a typical PIN structure. Their high aspect ratio can achieve strong optical coupling and light trapping: each nanowire is like an antenna, concentrating incident light into the active region, thus enhancing the local field intensity and absorption efficiency. Heteroepitaxial nanowires also relax lattice mismatch, enhancing junction quality and carrier lifetime.

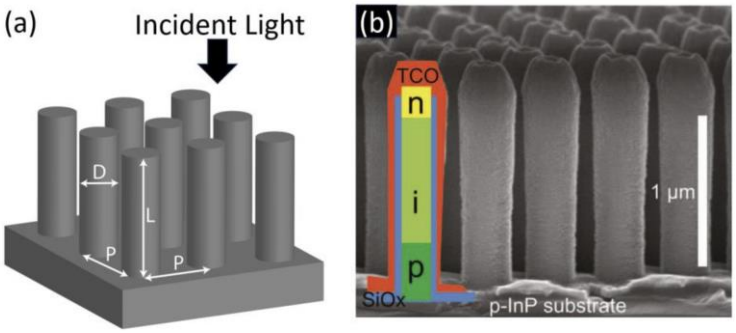

Figure 2.5. *(a) Schematic of an InP nanowire array showing D, L, and P. (b) SEM image of vertically grown PIN InP nanowires on a p-PIN substrate (adapted from [42]).*

In InAs nanowires, the surface Fermi level is pinned near the conduction band, forming an electron accumulation layer[43]. Even undoped wires act n-type and respond strongly to surface states. Upon illumination, surface charge redistribution dominates the photoresponse, modulating the channel potential through surface–channel coupling rather than bulk carriers. At low light intensity, electrons are trapped at surface states, leading to negative photoconductivity (NPC); as illumination increases, traps saturate and conduction rises, giving positive photoconductivity (PPC)[44][45]. A single InAs nanowire can thus switch from NPC to PPC depending on light intensity.

In contrast, InP nanowires have a wider band gap, lower dark current, and more controllable surface recombination. They typically show diode-like PPC behavior and fast temporal response in PIN structures, making them suitable as readout terminals[45]. Operating under small or reverse bias yields low noise photocurrents that reliably reflect interfacial changes. In hybrid systems, InAs acts as a light sensitive control terminal, while InP serves as a stable readout terminal converting potential variations into measurable currents.

2.1.3 Field Effect and Photoresponse Mechanisms

(1) Field effect and photogating modulation

Because InAs combines high mobility, a narrow band gap, and strong surface sensitivity, it is widely used in nanowire photo-FETs[46][47]. Its tunable NPC–PPC transition allows construction of photo controlled transistors whose channel is off in the dark and turned on by illumination.

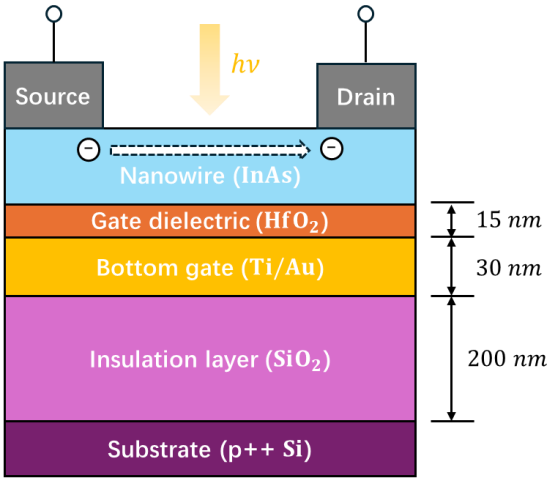

Figure 2.6. *Schematic of an InAs nanowire photo-FET showing the n-type channel, HfO_2 dielectric layer, Ti/Au bottom gate, and photon-induced charge modulation.*

As shown in **Fig. 2.6**, the nanowire lies on a 15 nm HfO_2 layer over a Ti/Au gate. Applying a gate voltage V_g induces an electric field that modulates the channel carrier density. In the dark, the drain current–voltage relation follows a simplified square-law form:

$$I_d = \mu C \frac{W}{2L}(V_g - V_{th})^2 \tag{2}$$

where C is the gate capacitance per area, μ the mobility, and V_{th} the threshold voltage. Under illumination, absorbed photons generate electron–hole pairs. Electrons enter the channel while holes are trapped at surface or interface states, creating a positive surface potential that shifts V_{th} toward lower voltage. This photogating effect enhances conductance and yields a clear threshold shift (**Fig. 2.7**)[48].

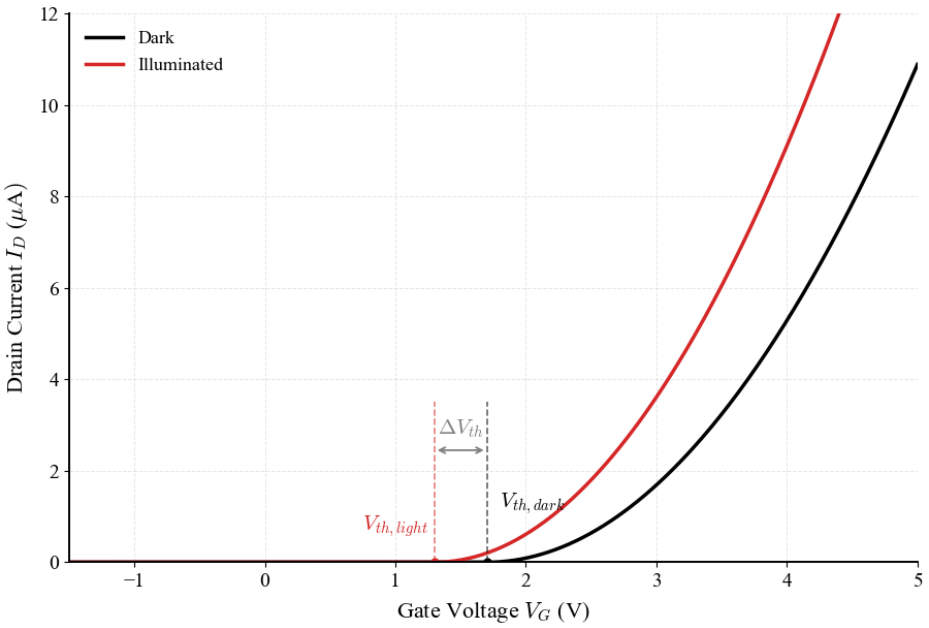

Figure 2.7. *Transfer curves of an InAs nanowire photo-FET under dark and illuminated conditions, showing threshold-voltage shift.*

This effect demonstrates the synergy between photoelectric and field phenomena. The photovoltage generated by absorbed light acts as an additional gate bias, modulating the channel current without external amplification. Since FETs are voltage controlled, small gate shifts produce large current changes, resulting in high gain photoresponse, the physical basis of the high sensitivity of nanowire photo-FETs.

(2) Quantum efficiency and photoresponse

Quantum efficiency (QE) quantifies how effectively a detector converts photons into collected carriers. It is given by

$$\eta = \frac{I_{ph} hc}{eP\lambda} \tag{3}$$

where I_{ph} is the photocurrent, P the incident optical power, e the electron charge, and λ the wavelength. The photoresponsivity R is

$$R = \frac{I_{ph}}{P} \tag{4}$$

which represents the current change per unit optical power. High R and η indicate efficient carrier generation and collection, crucial for neuromorphic optoelectronic devices.

2.2 Molecular Chemistry and Spectroscopy of DASA Dyes

Stimuli-responsive behavior is widespread in natural and synthetic systems, where structures or functions change in response to external cues. Inspired by these principles, researchers have developed a wide range of smart materials capable of reversible structural transformations when

triggered by external stimuli such as temperature[49], pH[50], or light[51]. Among these stimuli, light is particularly advantageous because it enables noncontact actuation, precise temporal control, and spatial selectivity[52][53]. Central to many light-responsive systems are photochromic molecules, which can reversibly switch between two distinct isomeric forms under illumination with different wavelengths.

One recently developed class of visible light photochromes is called Donor–Acceptor Stenhouse Adducts (DASAs), first reported by the Read de Alaniz group in 2014[54][55]. DASAs can change from a deeply colored open form to a colorless cyclic form under visible light, and then gradually revert to the colored state in darkness or under mild heating[56]. Compared with traditional UV responsive molecules, DASAs can be driven by low energy visible light, which is safer and more compatible with biological and soft matter systems[57].

2.2.1 Structure and Photoisomerization of DASAs

A DASA molecule consists of an electron donor (D), an electron acceptor (A), and a conjugated triene bridge connecting them, forming a D–π–A structure with extended conjugation along the molecular axis. This gives the molecule strong visible absorption and a characteristic color, as shown in Fig. 2.8 (left). When illuminated by visible light, the molecule undergoes a series of bond rotations and new bond formations, transforming from the colored linear form to the colorless cyclic form. The cyclization breaks the π-conjugation, shifting absorption into the UV range and causing the visible color to fade. The cyclic form is a thermally metastable state that spontaneously reopens in the dark, restoring the color[55]. This light-driven reversible reaction is the fundamental photochromic mechanism of DASAs.

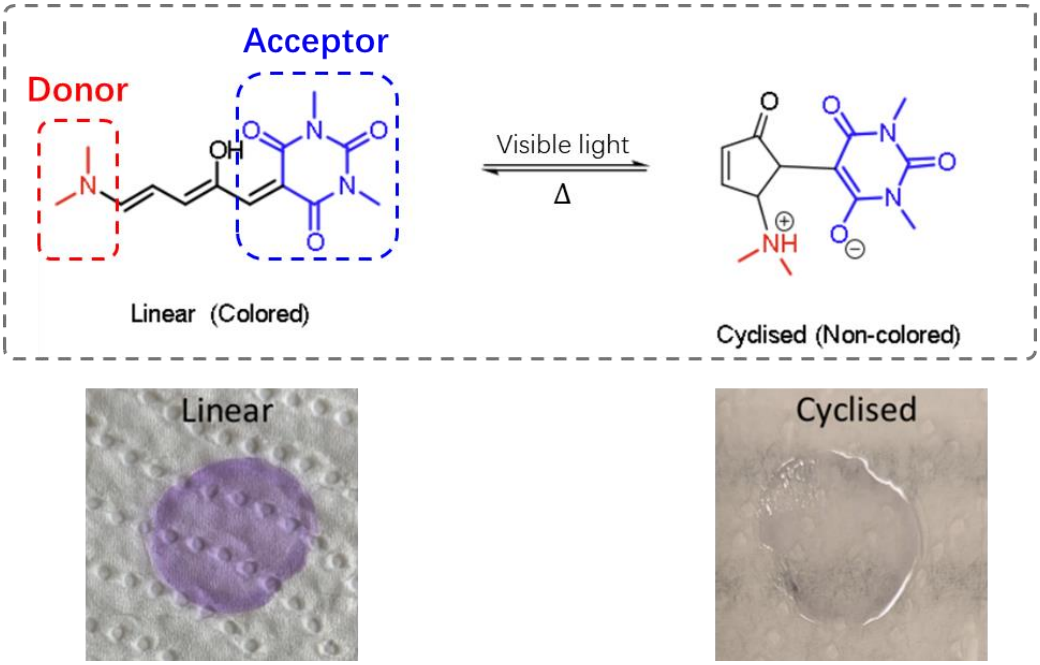

Figure 2.8. *Structure and photoisomerization of a DASA molecule. The donor, acceptor, and π-conjugated triene bridge form the D–π–A backbone. Left: linear (open) form, strongly colored; right: cyclic (closed) form, colorless.*

From a photochemical perspective, the process can be described as a light induced bond

reorganization between a global ground state (GS) and a metastable state (MS). The linear form, with its extended π system, is the lowest energy structure and absorbs visible light due to its strong charge transfer character. After photoexcitation, the molecule reaches an excited state (ES), where bond rotations and conformational rearrangements lead to closure of the ring and loss of conjugation. The resulting cyclic form is higher in energy and thermally unstable; in darkness or upon heating, it relaxes back to the open form through a thermally activated pathway.

Abbey and co-workers further clarified that this transformation involves the multi-step reaction sequence GS → ES → MS, followed by a thermal reaction of the reverse MS → GS[27]. Under continuous illumination, when the rates of photo closing and thermal opening are balanced, the photothermal stationary state (PTSS) can be reached. The equilibrium between the two forms depends on light intensity, temperature, and solvent polarity. Structural modifications also play a crucial role: stronger electron acceptors and longer conjugations can stabilize the open form, but slow down the ring-closing rate, forming a trade-off between responsiveness and stability.

2.2.2 Absorption, Bleaching, and Recovery Kinetics

The optical behaviour of DASA molecules can be studied by tracking the changes in the absorption spectrum over time. When exposed to light, the molecules undergo a series of events, including photon absorption, color bleaching, and a subsequent thermal return to the initial state. If a beam of light passes through a dye solution, the intensity of the transmitted light decreases exponentially with distance, as described by the Beer–Lambert law:

$$I = I_0 e^{-\varepsilon c l} \tag{5}$$

where I_0 and I are the incident and transmitted intensities, ε is the molar extinction coefficient, c is the molecular concentration, and l is the optical path length. The absorbance A is defined as $A = \log(I_0/I)$, which is directly proportional to the concentration of light-absorbing molecules. As illumination continues, the concentration of the colored open form decreases, resulting in the characteristic bleaching and a disappearance of color.

To study these processes more systematically, two DASA molecules, AP-066 and AP-048, were chosen as examples. Their different donor–acceptor structures and conjugation lengths lead to different absorption peaks and recovery times, which provides a useful comparison for understanding how molecular design affects photoswitching behavior. AP-066 uses a dimethylamine donor and dimethylbarbituric acid acceptor, showing a strong absorption at 568 nm with a molar extinction coefficient of $1.41 \times 10^5\ M^{-1} \cdot cm^{-1}$. Its closed form is relatively stable, with a thermal reopening rate constant of $k_{back} = 3.5 \times 10^{-3}\ s^{-1}$ ($\tau \approx 286\ s$). AP-048, using a 2-methylindoline donor and a pyrazolone acceptor, absorbs at 652 nm ($\varepsilon = 1.0 \times 10^5\ M^{-1} \cdot cm^{-1}$), but its closed form is less stable and recovers faster ($\tau \approx 55\ s$, $k_{back} = 1.8 \times 10^{-2}\ s^{-1}$). Table 1 summarizes their main optical and kinetic parameters.

Table 1.1. *Optical and kinetic parameters of the two DASA molecules used in this work.*

Molecule	Structural Composition	λmax (nm)	ε ($M^{-1} \cdot cm^{-1}$)	kback (s^{-1})	τback (s)	Optical and Stability Characteristics
AP-066	Donor = Dimethylamine Acceptor = Dimethylbarbituric acid 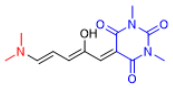	568 ± 2	1.41×10^5	3.5×10^{-3}	286	More stable (slow recovery)
AP-048	Donor = 2-methylindoline Acceptor = Pyrazolone 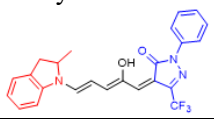	652 ± 3	1.0×10^5	1.8×10^{-2}	55	Less stable (fast recovery)

Note: Data are obtained from Abbey et al. as cited.; All kinetic values correspond to thermal recovery after light-off and were measured in toluene solution (room temperature, ca. $25 - 30\ °C$*). Reported* τ *values are time constants (*$\tau = 1/k$*); when needed, half-lifetimes follow* $t_{1/2} = \ln 2 \cdot \tau$.

The data show that molecular structure strongly affects both the absorption wavelength and the bleaching/recovery timescales.

Under continuous illumination, the linear form of DASA molecules gradually converts into the cyclic form, and the absorbance decays exponentially with time. Assuming the temperature remains constant during illumination, this process can be approximated as a first-order reaction, expressed as

$$\frac{dC_{\text{on}}}{dt} = -k_{\text{bleach}} C_{\text{on}} \tag{6}$$

Solving this differential equation gives $C_{on}(t) = C_{on,0} e^{-k_{bleach} t}$, where k_{bleach} is the rate constant of photo induced bleaching. According to the Beer–Lambert law, the corresponding time evolution of absorbance follows an exponential decay function: $A(t) = A_0 e^{-k_{bleach} t}$. When illumination is stopped, the system in its metastable cyclic state begins a *thermal recovery process* and gradually reverts to the open linear form. The absorbance recovery can then be described as $A(t) = A_0(1 - e^{-k_{back} t})$, where k_{back} is the thermal recovery rate constant, and $\tau_{back} = 1/k_{back}$ represents the characteristic recovery time of the system. Essentially, a larger k_{back} means a faster recovery but lower thermal stability.

Figure 2.9 illustrates this behavior for three DASA derivatives in toluene. Panel (a) shows their normalized absorption spectra before and after bleaching, while panel (b) displays the corresponding absorbance–time curves under illumination and dark conditions. All three samples exhibit typical exponential bleaching and recovery kinetics. It shows that AP-048 has a higher bleaching rate constant than AP-066, and a faster recovery, which is correlated with the stronger electron-withdrawing ability of its acceptor group.

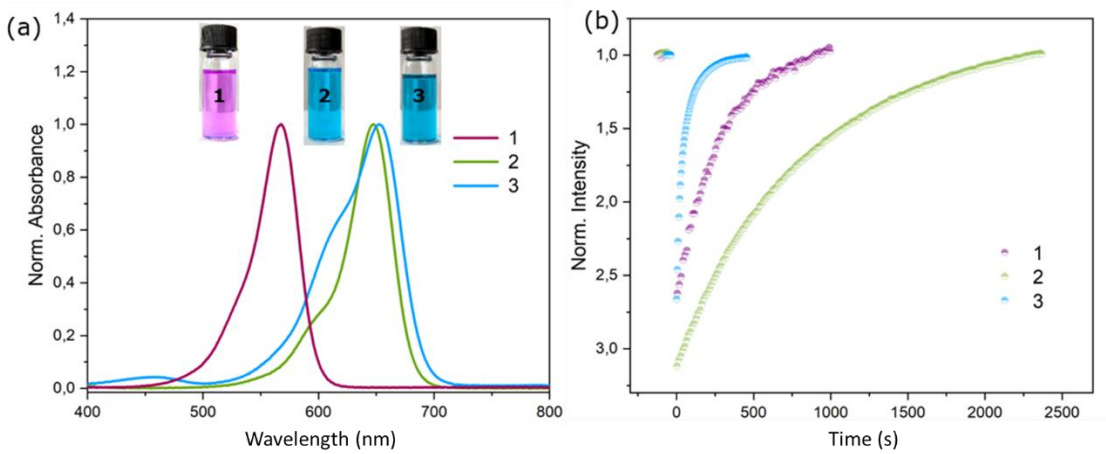

Figure 2.9. *(a) Normalized absorption spectra of AP-066, AP-007, and AP-048 in toluene. (b) Time-dependent bleaching and recovery under light and dark conditions (data from Abbey et al.[27]).*

To describe both the bleaching and recovery processes in a unified form, the total molecular concentration can be written as $c_{tot} = c_{on} + c_{off}$. Combining this with the Beer–Lambert law, the light intensity inside the sample can be expressed as

$$I(t) = I_0 \times 10^{-\varepsilon l[c_{\text{tot}} - c_{\text{off}}(t)]} \tag{7}$$

where $c_{off}(t)$ is the time dependent concentration of the cyclic form. When both photobleaching and thermal recovery occur simultaneously, the temporal evolution of the cyclic-state concentration follows

$$\frac{dc_{\text{off}}}{dt} = I_0(t)\Phi\left(1 - 10^{-\varepsilon l[c_{\text{tot}} - c_{\text{off}}(t)]}\right) - k_{\text{back}} c_{\text{off}}(t) \tag{8}$$

In this equation, the first term represents the formation of the cyclic state under illumination, where Φ is the quantum yield of photoisomerization; the second term corresponds to the thermal back reaction. By numerically solving this equation, the absorbance time curves under steady illumination or dark recovery can be accurately reproduced, and the results agree well with the experimental data reported by Abbey *et al.*[27]. Their findings confirm that this kinetic model has successfully described the photobleaching and thermal recovery dynamics of DASAs under different illumination conditions.

2.2.3 Polarization Dependence of Molecular Absorption

The interaction between light and a molecule depends on the orientation of its transition dipole moment relative to the electric field of the light. For linear molecules or D–A-type structures like DASAs, the transition dipole moment μ is typically aligned with the molecular axis[58]. If the electric-field vector E makes an angle θ with μ, the absorption intensity follows:

$$I(\theta) \propto | E \cdot \mu |^2 = E^2 \mu^2 \cos\theta^2 \tag{9}$$

When the molecular axis is parallel to the electric field ($\theta = 0°$), absorption is strongest; when perpendicular ($\theta = 90°$), it is weakest. **Figure 2.10** illustrates this concept. In a toluene solution (**Fig. 2.10a**), DASA molecules are randomly oriented, so absorption is isotropic and independent of

polarization[59].

When incorporated into a polymer matrix or attached to a nanowire surface (**Fig. 2.10b**), molecular motion is restricted. Van der Waals interactions and $\pi - \pi$ stacking can cause molecules to align partially along the substrate, leading to *partial orientation*. As a result, the overall absorption becomes polarization dependent. **Figure 2.10c** defines θ as the angle between μ and E; the effective absorption component is proportional to $\cos^2\theta$, explaining why polarization sensitive behavior emerges in thin films or dye-nanowire interfaces[60][61].

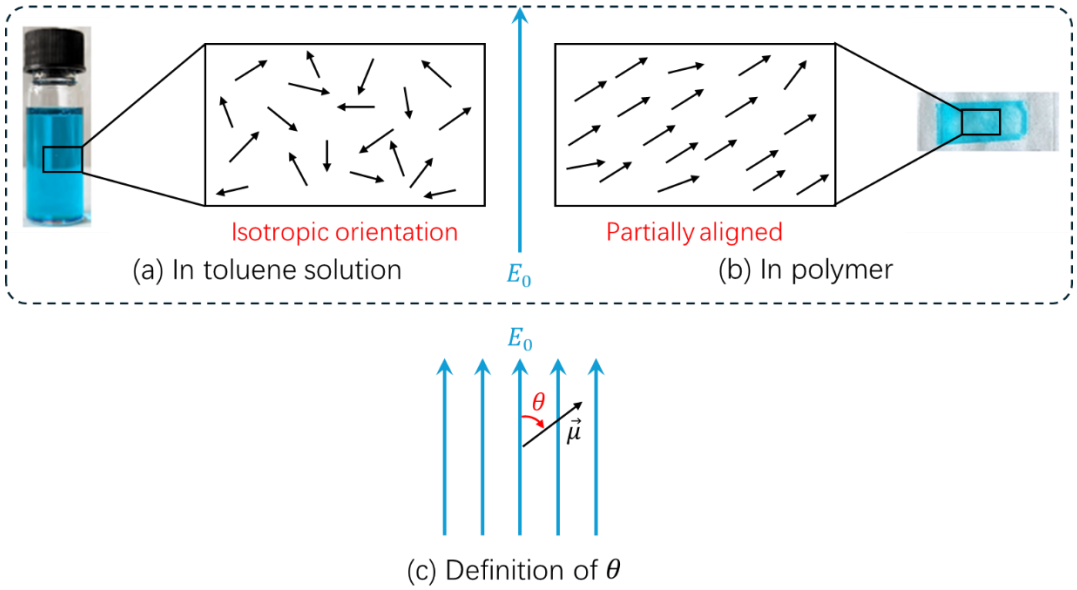

(c) Definition of θ

Figure 2.10. *Schematic of molecular orientation and polarization dependence.* (a) Random orientation in toluene solution (isotropic absorption). (b) Partial alignment in polymer or at the nanowire interface (anisotropic absorption). (c) Definition of the angle θ between transition dipole moment μ and field vector E.

2.3 Neuromorphic Memory and Synaptic Plasticity

In neuromorphic systems, the synapse is the fundamental unit responsible for learning and memory. Its weight determines the strength of signal transmission between neurons. In biological neural networks, synaptic plasticity refers to the ability of synaptic strength to change in response to external stimuli, allowing information to be stored or forgotten over time. As discussed in **Chapter 1** (**Fig. 1.1**), biological neural networks differ from von Neumann architectures in that computation and memory are co-located within interconnected neurons and synapses.

To further illustrate the biological basis of information transmission, **Fig. 2.11** shows a schematic of two connected neurons forming a synapse. Neuron 1 releases neurotransmitters at the axon terminal, which are received by the dendrite of Neuron 2, creating a synaptic junction. The strength of this connection determines the efficiency of signal transfer and serves as the physical foundation of synaptic plasticity in neuromorphic systems.

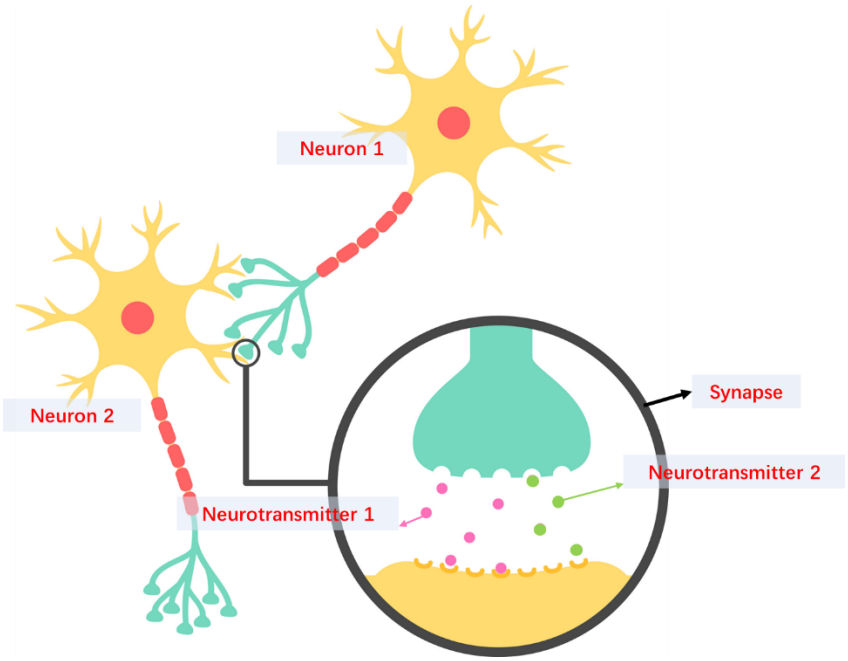

Figure 2.11. *Schematic illustration of two connected neurons showing neurotransmitter release and synaptic coupling (adapted from* ***Fig. 1.1b****).*

Inspired by this principle, artificial synaptic devices have been designed to mimic biological learning behavior. Among them, optical synapses use light as the control signal. Light offers fast response, high bandwidth, and noncontact control, making it ideal for adjusting synaptic weight through combined optical and electrical effects. In this study, the hybrid dye–nanowire device uses the reversible photoisomerization of DASA molecules together with carrier modulation in nanowires to achieve precise control of the current that represents the synaptic response.

2.3.1 Synaptic Plasticity and Memory Mechanisms (STP and LTP)

Synaptic plasticity is the basic physiological process that enables learning and memory in the nervous system[62]. It describes the reversible adjustment of synaptic transmission efficiency when a stimulus is applied. Experimentally, this change is often observed as the variation of the post synaptic current (PSC), which reflects the time dependent evolution of synaptic weight $w(t)$.

According to the duration of modulation, plasticity can be divided into short-term plasticity (STP) and long-term plasticity (LTP). STP lasts from milliseconds to minutes and is usually related to the accumulation and release of ions or carriers at interfaces. LTP, in contrast, may last for hours or even days, corresponding to more permanent structural or electronic modifications in the synapse[63]. The general form of synaptic weight variation can be written as

$$w(t) = w_0 + f(S,t) \tag{10}$$

where w_0 is the initial weight, and $f(S,t)$ describes the change under the applied stimulus S as a function of time. When $f(S,t)$ decays rapidly after the stimulus is removed, the system exhibits STP; if the change can be maintained for a long time, it corresponds to LTP. This simple model provides a unified way to understand the different synaptic behaviors observed in artificial equipment.

2.3.2 Dynamic Reversible Memory Model

In the hybrid dye–nanowire synapse, the current response to optical stimulation is neither instantaneous nor permanent. It is controlled by two competing processes: photobleaching of DASA molecules and their thermal recovery (i.e., spontaneous recovery driven by thermal fluctuations). When exposed to light, DASA molecules change from an open state to a closed state. This immediately increases the channel current. When the light goes off, the closed molecules gradually return to the open state, and the current decays to its steady state value.

According to the kinetic model described in Section 2.2 (Eq. 8), the change of molecular concentration over time reflects the competition between bleaching and recovery. Assuming that the device current $I(t)$ is proportional to the ratio of cyclic molecules $c_{off}(t)$, the current response can be expressed as

$$I(t) = I_0 + \alpha \frac{c_{\text{off}}(t)}{c_{\text{tot}}} \tag{11}$$

where I_0 is the dark current and α is the proportional constant, indicating the modulation intensity caused by the interface dipole layer. Substituting $c_{off}(t)$ in Eq. (8), the current change rate can be written as

$$\frac{dI(t)}{dt} = k_{\text{bleach}}[I_{\text{sat}} - I(t)] - k_{\text{back}}[I(t) - I_0] \tag{12}$$

Here, k_{bleach} denotes the rate constant of photo-induced bleaching, describing the rate at which the photocurrent increases under illumination. k_{back} is the thermal recovery rate, which characterizes the speed at which the system returns to its initial state after illumination. I_{sat} represents the saturated current under continuous light exposure, while I_0 is the dark current before illumination. This model describes the dynamic evolution of device current (or optical conductance) during and after light stimulation. When the light is turned on, the first term dominates, and the system exhibits a gradual increase in photocurrent. When the light is turned off, the second term dominates, which leads to recovery. The ratio of these two constants determines the memory retention or memory behavior of the system. When $k_{bleach} > k_{back}$, the system maintains its excited state for a longer time, showing slower relaxation and long-lasting memory, which is similar to long-term plasticity. On the contrary, when k_{back} is larger, the current quickly returns to the initial state, indicating that there is short-term plasticity that is a short-lived and easy to reverse.

Therefore, the concept of dynamic reversible memory can be regarded as an extension of the molecular kinetics model in the field of electricity. Its effective time constant

$$\tau_{\text{eff}} = (k_{\text{bleach}} + k_{\text{back}})^{-1} \tag{13}$$

serves as a key parameter to describe the time behavior of the synaptic current and the duration of memory. This model links the molecular optical isomerization dynamics with the device-level electrical response, providing a theoretical basis for the analysis of the rising and decaying behaviors observed in subsequent experiments.

2.4 Multichannel Optical Modulation in Dye–Nanowire Synapses

Optical synaptic devices can regulate signal transmission through light to achieve learning and memory functions similar to those in biological systems. Compared with conventional electronic synapses, optical ones have faster response speed, lower energy consumption and the potential for parallel multi-channel processing. In this work, the hybrid structure composed of dye molecules and nanowires shows wavelength and polarization-dependent tunability, demonstrating the potential of multi-channel synaptic plasticity.

2.4.1 Dual-wavelength Spectral Response

Two DASA molecules with different absorption peaks are introduced into the system: AP-066 (absorption peak is around 568 nm) and AP-048 (absorption peak is around 652 nm). The separation of the absorption bands of the two species minimizes the energy transfer between them. As a result, under different illumination wavelengths, each type of molecule mainly undergoes its own photoisomerization process. This wavelength selectivity enables the system to respond to different spectral channels independently.

Under optical excitation, the isomerization of AP-066 and AP-048 molecules will cause the interfacial charge transfer inside the nanowire–dye composite, leading to the optical modulation of the current. If the two illumination wavelengths are λ_1 and λ_2 respectively, the total photocurrent of the device can be expressed as:

$$I_{\text{total}}(t) = w_1 I_1(t, \lambda_1) + w_2 I_2(t, \lambda_2) \tag{14}$$

where w_1 and w_2 represent the weight factors corresponding to the two wavelength responses, reflecting the overall contribution of photoexcitation to current modulation. Because two dye molecules absorb light independently in their characteristic wavelength range, the system shows distinct wavelength selectivity. However, in practical applications, there may still be a certain degree of crosstalk, mainly due to the partial overlap of spectral bands, scattered light and local heating effects. Nevertheless, this phenomenon does not significantly affect the independence of each optical channel, and it is confirmed that the hybrid system can respond to multiple optical inputs at the same time.

2.4.2 Polarization-dependent Modulation in Single-dye Channel

For samples containing AP-048 molecules, a clear polarization-dependent response was observed. The transition dipole moment of the DASA molecule is located on its molecular axis; thus, when the polarization direction of the incident light is parallel to the molecular axis, the absorption reaches the maximum value, while perpendicular polarization leads to the minimal absorption. If θ represents the polarization angle, then the photocurrent can be written as:

$$I(\theta) = I_{\parallel} \cos\theta^2 + I_{\perp} \sin\theta^2 \tag{15}$$

By rotating the polarization direction ($0° - 90°$), different photocurrent amplitudes can be obtained. This indicates that the DASA molecules are partially aligned along the surface of the nanowire to form an oriented arrangement. The coupling between molecular dipoles and the polarized

photoelectric field enhances the polarization correlation response, resulting in measurable anisotropy.

Chapter 3 – Methods

This chapter explains the experimental methods and analytical approaches used in this study, aiming to provide a technical basis and interpretation framework for subsequent results and discussions.

The research mainly focuses on two aspects:
(1) the optical and kinetic behavior of photochromic dyes, especially DASA derivatives AP-066 and AP-048;
(2) the photo-response of the hybrid system formed by coupling these dyes with III–V nanowire devices.

It should be noted that the nanowire devices used in this study were not manufactured from scratch. The III–V nanowire samples (such as InP and InAs) were grown, transferred, and electrode patterned by a cooperative team. Therefore, this chapter does not include details such as epitaxial growth conditions, doping concentration or metal contact manufacturing. The delivered devices already have electrical functions. The focus of this work is on how to introduce the DASA molecular layer on their surfaces and achieve controllable optical writing and electrical reading.

The design goal of the characterization methods is to keep its complexity at a repeatable and easy-to-apply level. Compared with high-sensitivity measurements of single nanowires, this study focuses on system-level behavior, that is, whether the combination of the molecular layer with the entire nanowire array can exhibit synaptic-like functions such as writing, retention, decay, and reading.

For this purpose, several key experimental tools were used:
• a controllable multi-wavelength illumination system (G2V Solar Simulator and LED modules) is used to apply optical stimulation and define “Write” and “Read” events;
• an integrating sphere spectroscopic system is used to record the change of the transmission spectra of the dye layer over time, and extract kinetic constants for photobleaching and recovery;
• a microprobe station is used in combination with a Keithley source meter to record the current changes under illumination and determine whether the molecular state can be read electrically.

The overall goal of these methods is to use combination of optical and electrical measurements to reveal the reversibility of DASA molecules in the solid state and to explore the possibility of achieving controllable optical writing in hybrid nanowire devices.

3.1 Preparation of DASA–PAMS Solution and Film Formation

This study aims to introduce a reversible photochromic response layer on a solid nanowire array platform. The photo-responsive molecules used here are two DASA compounds, AP-048 and AP-066. Under visible light illumination, DASA molecules can change from open form to closed form: open form shows extended conjugation and visible absorption, while the closed form loses conjugation and presents colorless or almost colorless. Ideally, this process is reversible. However, in solid environments, molecular interactions become stronger and conformational motion is limited,

making the closed form more stable and often preventing full recovery to the open form. As a result, the optical response becomes gradually irreversible or weakened.

To maintain reversibility under solid-state conditions, the DASA molecules were dispersed and fixed in a poly(α-methylstyrene) (PAMS) matrix. PAMS provides a non-polar local environment and a flexible 3D polymer network, allowing molecular scale embedding and stabilization of the dyes.

This section describes the design principles and actual preparation of the composite system, including the selection of solvent, preparation of dye solutions, deposition on nanowire devices, drying and curing conditions, and the morphology and stability of the resulting film. All processes were carried out under ambient temperature and low light conditions to avoid premature photoisomerization before the film was fully solidified.

3.1.1 Design of Solvent System, PAMS Matrix, and Local Environment

DASA molecules are not naturally suited for solid-state operation. The challenge is not only the lack of molecular mobility after solidification but also the polarity of the surrounding medium. In polar environments, the closed (colorless) form of DASA is stabilized by strong dipole–dipole interactions, making the molecule tend to remain in the closed configuration after illumination, resulting in incomplete or irreversible bleaching. This is a major reason why many DASA compounds show poor reversibility in water or polar polymer matrices[55]. In contrast, in non-polar environments, the closed form is not additionally stabilized, allowing the molecule to spontaneously return to the open form once the external light stimulus is removed. In other words, the “reversibility” of DASA in solids is not a built-in property but must be maintained by controlling its local environment.

Based on this principle, PAMS was chosen as the host polymer. Its hydrocarbon backbone makes it chemically inert and non-polar[61]. After drying, PAMS does not crystallize but forms an amorphous, entangled polymer network. During solvent evaporation, DASA molecules become gradually embedded and fixed within nanoscale cavities of this network. **Figure 3.1** shows the diagram of DASA molecules dispersed in the PAMS matrix. In this conceptual model, the polymer network is represented as hexagonal cavity occupied by individual AP-048 or AP-066 molecules. It should be noted that this figure is only a simplified conceptual representation, not a real microscopic structure. In fact, PAMS is an amorphous polymer. Its chains are randomly entangled during solvent evaporation to form a disordered 3D network with different local densities and orientations. These networks produce a series of non-polar microenvironments, which play the role of “approximate cavity”[60]. During the solvent drying process, DASA molecules are fixed in these regions in a dispersed state rather than aggregated state. This irregular yet homogeneous distribution effectively reduces intermolecular interactions and suppresses aggregation-induced quenching or phase separation[55][56]. Meanwhile, because the polymer backbone does not provide strong polarity or hydrogen bonding, the closed form of DASA is not energetically stabilized and can recover to the open form once illumination stops.

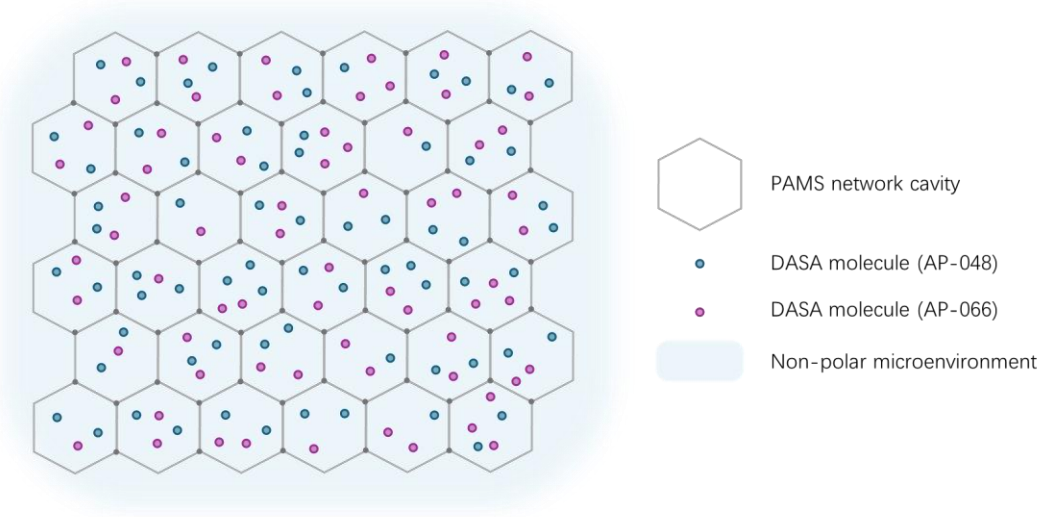

Figure 3.1. *Schematic illustration of DASA molecules distributed within the PAMS network. The polymer network is shown as regular hexagonal cavities representing local microcavities formed inside PAMS. DASA molecules (blue: AP-048; purple: AP-066) are randomly dispersed in these nonpolar regions, avoiding aggregation and maintaining reversible photoresponse in the solid state.*

To ensure that the PAMS layer could attach uniformly onto the nanowire array surface instead of forming uncontrolled bulk residues, a mixed-solvent system of dichloromethane (DCM) and toluene was used. The solvent ratio was DCM:toluene = 9:1 (v/v), with 15 wt% PAMS pre-dissolved in the mixture.

First, DCM has a low boiling point ($39.6\ °C$), which allows it to evaporate quickly near room temperature, helping the liquid film shrink and fix its shape shortly after deposition. Secondly, the boiling point of is much higher ($110.6\ °C$), but with the evaporation of DCM, the toluene will be partially taken away, leading to gradual solidification instead of sudden liquid-to-solid transition. After a few minutes, the film slowly becomes more viscous, contracted, and finally stabilized. This gradual drying process can reduce internal mechanical stress and minimize defects such as bubbles, shrink lines, or edge curls. Finally, toluene is a non-polar aromatic solvent, which helps to maintain the open form of DASA during preparation and improve the solubility of PAMS, preventing macroscopic phase separation.

It is worth noting that PAMS is not just a structural “support layer” at the macro level, it directly defines the operating boundary conditions of solid-state DASA. The polymer network limits molecular movement, but does not completely freeze it. This phenomenon is often seen in amorphous polymer matrix that retains local free volume and allows limited segmental movement[59]. Even after solidification, the network still maintains a certain degree of flexibility, allowing DASA molecules to perform local conformational movements without fixing them completely as in rigid or strongly polar matrix. This condition of “locally mobile but globally stable” is the microscopic basis for the reversible photo-response observed in later optical measurements.

3.1.2 Preparation, Deposition on Nanowire Devices, and Drying Process

Dissolve AP-048 and AP-066 in the above PAMS/DCM/toluene mixture respectively, with a target concentration of 1 mM, so as to obtain two working solutions of completely different colors (blue for AP-048, purple for AP-066). During the dissolution process, the two dyes show different behaviors: AP-066 dissolves slowly and requires longer stirring to form a uniform solution. This slower dissolution rate is attributed to stronger intramolecular interaction, which is conducive to the aggregation of molecules in low-polar solvents. Prolonged stirring or slight ultrasonic agitation gradually breaks these bonds, yielding an optically uniform solution. This difference is also related to the later comparison of their optical absorption characteristics, which will be discussed in the results chapter.

After the preparation is completed, the nanowire array sample is placed horizontally. Deposit the DASA–PAMS solution directly on the sample by drop-casting: slowly add multiple small droplets from above to make the liquid diffuse spontaneously. The sample is kept horizontal during the deposition process, without tilting or rotating drying. This detail is not arbitrary, it is directly related to later optical and electrical measurements. If the film is too thin, the surface density of active molecules will be too low, and the contrast of optical or electrical signals will be too weak to be detected. Overthinning may also cause some areas to be not covered, resulting in poor reproducibility between samples. Although techniques such as spin-coating could produce more uniform films, they usually produce thinner layers, which would require higher dye concentrations to maintain sufficient optical contrast. Therefore, we choose the drop-casting method to ensure the complete coverage of the nanowire array and achieve stable and reproducible measurements.

After the film is evenly spread, transfer the sample to the temperature-controlled hot plate and keep it at $35\ °C$ for about 5 minutes. There are two reasons for choosing this temperature. First of all, it is close to but slightly below the boiling point of DCM, enabling rapid evaporation without violent bubbles or pitting. Secondly, in the process of continuous evaporation of DCM, toluene is also gradually removed, so that the liquid film can smoothly transition to a semi-solid state. If the temperature exceeds about $40\ °C$, local microbursts of vapor may occur, causing cracking, curling of edges or thickening. Practice has proved that $35\ °C$ is repeatable compromise: the temperature is mild enough to preserve film integrity, and at the same time, it is high enough to fix the organic layer into a uniform and continuous coating in a few minutes.

After hot plate treatment, the sample is placed in darkness at room temperature for several hours to escape the residual solvent and further stabilize the polymer network. At this stage, the entanglement between PAMS chains is gradually fixed, and DASA molecules is trapped in a local non-polar cavity. The dark environment is very essential. It is not to prevent heating, but to avoid triggering photoisomerization before it is fully cured. Too early illumination could lead to different proportions of local isomers, resulting in uneven color distribution and the introduction of baseline offset in subsequent measurements.

After drying and stabilizing, the film shows a uniform and continuous covering under the microscope. No accumulation, crystallization or cracks have been observed, indicating that the solvent evaporation occurs evenly on the surface. This morphology is reproducible between samples

prepared under identical solvent composition, volume, and thermal conditions. The obtained film has mechanically stability and optically activity, and can be directly used for subsequent optical transmission, integrating sphere, and electrical measurements.

Figure 3.2 illustrates the DASA–PAMS sample preparation and deposition process. The left panel shows the preparation of the DASA–PAMS working solution. The upper right schematic illustrates drop casting on a sapphire substrate, forming a uniform thin film for optical transmission and bleaching tests. The lower right schematic shows the same solution deposited on a nanowire array device for electrical measurements of the dye–nanowire hybrid system. Controlled heating and dark storage allow gradual solvent evaporation, leading to stable DASA–PAMS solid films on both types of substrates. The figure serves as a conceptual diagram, not representing the actual scale or film morphology.

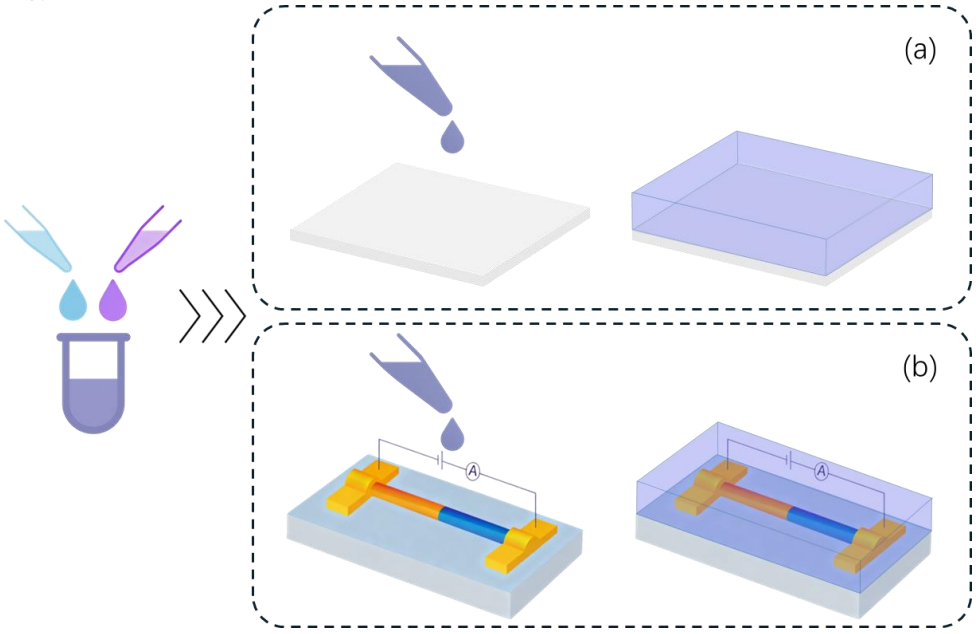

Figure 3.2. *Schematic illustration of the preparation and classification of DASA–PAMS films. The left panel shows the preparation of the DASA–PAMS dye solution; (a) drop casting on a sapphire substrate for optical measurements; (b) drop casting on a nanowire array device for electrical measurements. For clarity, only a single nanowire is illustrated in the figure, while the actual device is composed of a nanowire array.*

3.2 Optical and Electrical Characterization

To systematically study the photo-response of DASA films and their behavior on nanowire array devices, two complementary measurement techniques are adopted: optical transmission spectroscopy and current–time response measurement. The first method analyzes the light absorption, bleaching, and recovery of solid-state DASA, while the second investigates the current change of nanowire arrays under illumination and its potential photo-modulation mechanism. Both experiments were conducted under controlled LED illumination provided by the G2V solar simulator, ensuring consistent light conditions. All measurements were performed at room temperature and low humidity to minimize environmental effects on the open/closed-state equilibrium of the dyes.

3.2.1 Optical Measurements

(1) System configuration and measurement principle

The optical spectra of DASA films were measured using a Bentham VC-610 double-monochromator integrating-sphere system. The setup includes a composite light source (xenon and tungsten-halogen lamps) driven by stable current modules, a dual monochromator, an integrating sphere, and a current amplifier with a lock-in detector, as shown in **Figure 3.3**. The broadband light from the two Bentham 610 power modules is spectrally dispersed by the monochromator and then directed into the integrating sphere. The sample is mounted at the entrance port of the sphere, and the transmitted light is collected by the detector.

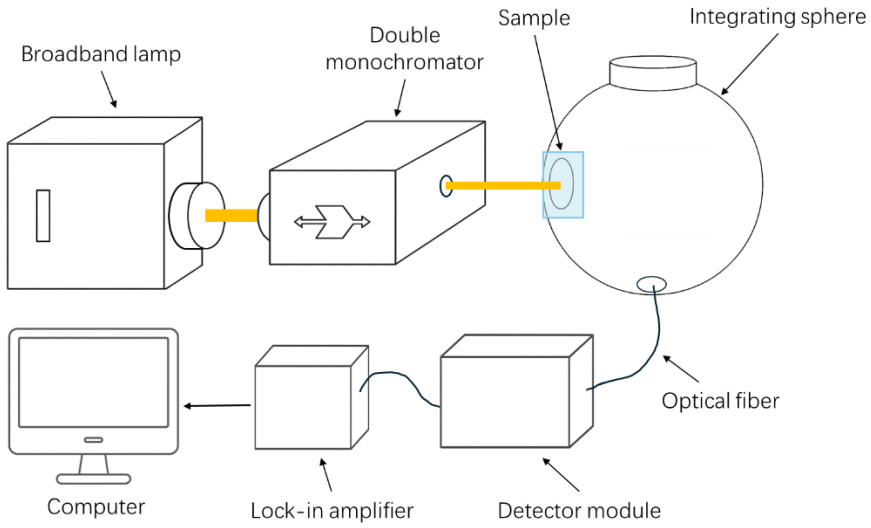

Figure 3.3. *Schematic of the optical transmission measurement setup. Broadband light is filtered by the double monochromator and directed onto the sample at the entrance of the integrating sphere. The diffusely mixed transmitted light is collected through the detector port via an optical fiber and recorded by the detector and lock-in amplifier.*

Inside the sphere, the filtered beam undergoes multiple diffuse reflections from the highly reflective inner coating. These repeated reflections mix the light evenly and eliminate any dependence on the incident angle. Therefore, the detector records the total transmitted flux passing through the sample, not the light from a single propagation direction.

In the process of data acquisition, the signal of each wavelength point is converted into incident light power according to the known responsivity of the detector. This responsivity provided in the official calibration document can correct the change of photoelectric conversion efficiency with wavelength and ensure accurate transmission rate calculation. The overall measurement workflow and system setup are illustrated in **Figure 3.4**.

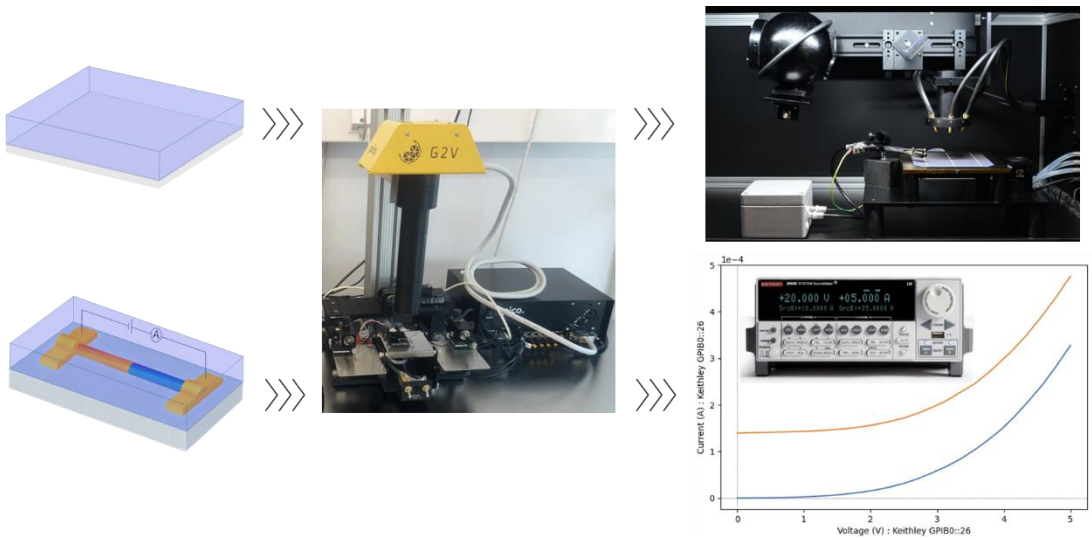

Figure 3.4. *Schematic diagram of optical and electrical measurement devices. The upper path shows the optical transmission test of DASA films on sapphire substrates (Bentham integrating sphere system). The lower path shows the electrical measurement of DASA-nanowire hybrid devices using a Keithley 2400 SourceMeter. Both types of measurements are carried out under LED illumination from the G2V module to ensure consistent light conditions.*

(2) Reference baseline and measurement consistency

In this system, the reference spectrum is used as an "air reference", that is, the transmission signal is measured without any sample. This approach simplifies the comparison between samples but introduces a small systematic error caused by reflection and scattering at the substrate interface. For sapphire substrates, the relatively high refractive index (about 1.7–1.8) leads to noticeable Fresnel reflection on both surfaces, which may cause a baseline offset by up to tens of percent, depending on the angle of incidence distribution and the geometry of the integral sphere. Using a blank substrate as a reference could partially correct these reflection and scattering effects; however, differences in substrate thickness and surface treatment may introduce new artifacts such as interference fringes. Since this study focuses on the relative transmission change of the samples before and after illumination, rather than absolute transmission values, the air reference method is consistently used for all measurements to ensure comparability and reproducibility of the spectra.

(3) Light source stability and normalization strategy

To evaluate the output stability of the Bentham system after the light source was turned on, reference spectra are continuously recorded without a sample. During the first 15 minutes, the transmission signal increased slowly and reached a stable level after about 20 minutes. Representative results are shown in **Figure 3.5**: the average transmission in the 500–650 nm range can be fitted with a single exponential model,

$$y(t) = y_{\infty} - Ce^{-\frac{t}{\tau}} \tag{16}$$

yielding a time constant of $\tau \approx 590\ s$, which characterizes the stabilization rate of the light source from startup. According to the model, the system reaches about 63% of its steady state level after roughly 10 minutes and 90–95% after 20–30 minutes. The fitting confirms that the lamp output

gradually approaches stability rather than reaching it abruptly.

In practice, halogen (or xenon-arc) lamps still exhibit slow intensity drift due to filament and housing heating, making perfectly constant illumination unrealistic. Since this work emphasizes relative transmission variations rather than absolute intensity, full stabilization of the light source was not required. All measurements were started after approximately 20 minutes of warm-up, and in-situ normalization was applied (each sample spectrum was divided by its corresponding reference spectrum) to eliminate slow source drift and ensure reliable comparison of relative spectral changes.

$$Norm(\lambda, t) = \frac{T_{sample}(\lambda, t)}{T_{ref}(\lambda, t)} \tag{17}$$

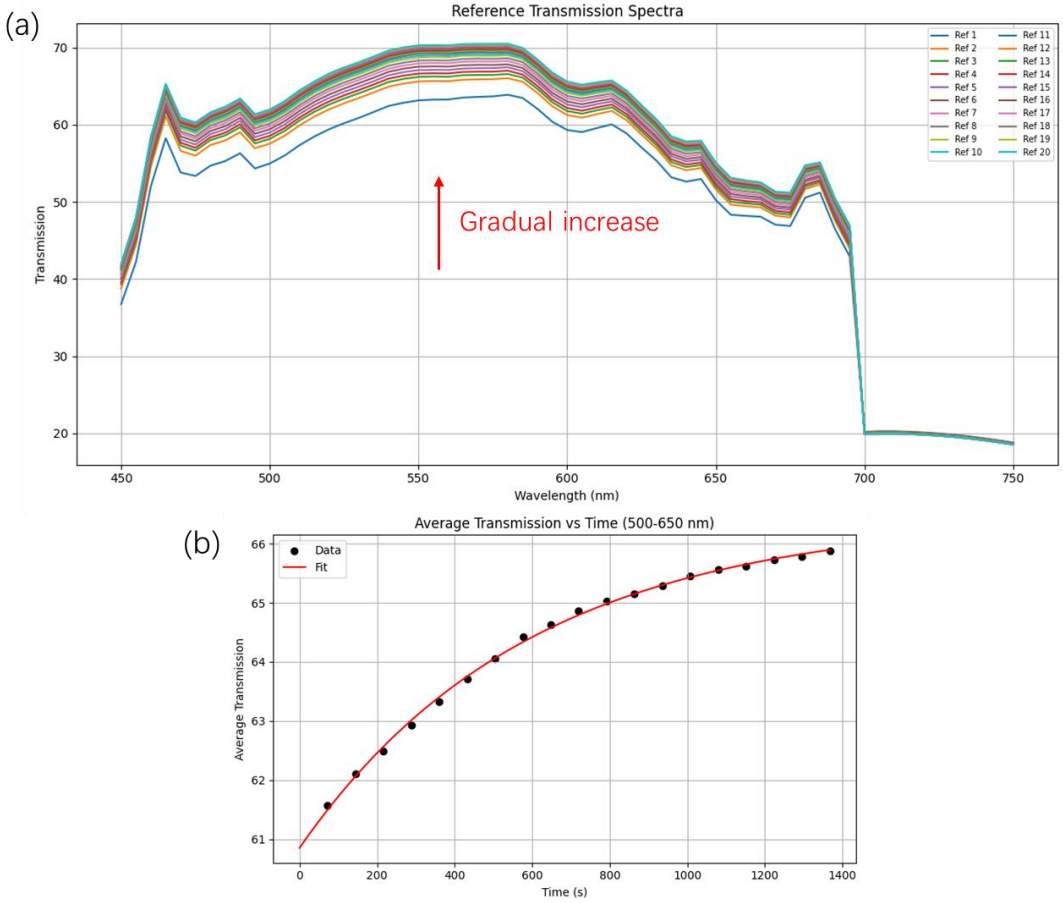

Figure 3.5. *Evaluation of light source stability. (a) Twenty consecutive reference spectra recorded after the Bentham system was turned on. (b) Average transmission in the 500–650 nm range as a function of time with exponential fitting.*

(4) Photobleaching and spectral acquisition

In the photobleaching experiments, each sample was first illuminated by selected LED channels of the G2V solar simulator for 2–3 minutes. The G2V system provides multiple wavelength channels, with illumination intensity controlled through the software parameter Solar Simulator Value. Because the spectral ranges of different LED channels partially overlap, two channels were chosen to match the main absorption bands of AP-048 and AP-066, respectively, to induce isomerization.

After bleaching, the sample was immediately transferred to the Bentham system for transmission measurement and recovery monitoring. Since DASA molecules embedded in the PAMS matrix can reversibly switch between open and closed forms, the transmission gradually returns toward its initial value over time. To record this process, repeated spectral scans were performed immediately after the light was turned off, yielding the temporal recovery curves.

3.2.2 Electrical Measurements

(1) Device structure and measurement configuration

The electrical response of the nanowire array devices was measured using a Keithley 2400 SourceMeter. From an electrical-circuit standpoint, each silicon nanowire behaves as an individual junction element connecting the Si substrate to the top metal pad. Because all nanowire bottoms share the same Si substrate and all tops merge into a common output electrode, the nanowire array can be represented as a large number of parallel junctions. The total current recorded by the SourceMeter therefore corresponds to the sum of the currents flowing through all nanowire channels.

To clarify this circuit interpretation, **Figure 3.6** shows a simplified equivalent circuit, where each nanowire is modelled as a junction connected in parallel between the Source (grounded Si substrate) and Drain (top metal pad). This parallel network representation highlights that any light-induced modulation caused by the DASA molecular layer affects all nanowire channels simultaneously and contributes collectively to the measured current.

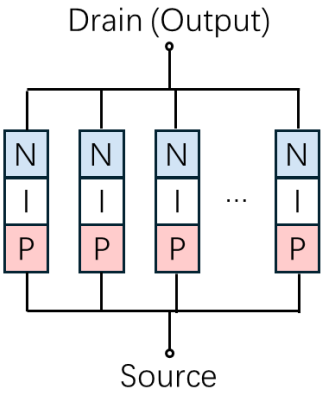

Figure 3.6. *Equivalent circuit of the nanowire array device. Each nanowire is represented as an PIN junction element, and all channels are connected in parallel between the drain electrode and the Si substrate.*

Figure 3.7 provides the actual device structure. The left panel shows an optical photo of the nanowire device chip, which contains multiple identical nanowire array units. One of the units (yellow highlighted part) is used for all electrical measurements. The right panel illustrates the geometry of the selected array: the grounding probe contacts the Si substrate as the Source pole, and the second probe touches the long rectangular metal pad on the right side of the array, serving as the Drain pole. In this configuration, current flows from the nanowire tips to the output electrode and then to the measurement terminal.

The nanowire array is coated with a DASA molecular film, which can regulate carrier transport

under illumination. Since all nanowires work in parallel, the measured current reflects the integrated response of the entire array, enabling the device to operate as a multi-channel photo-modulation platform.

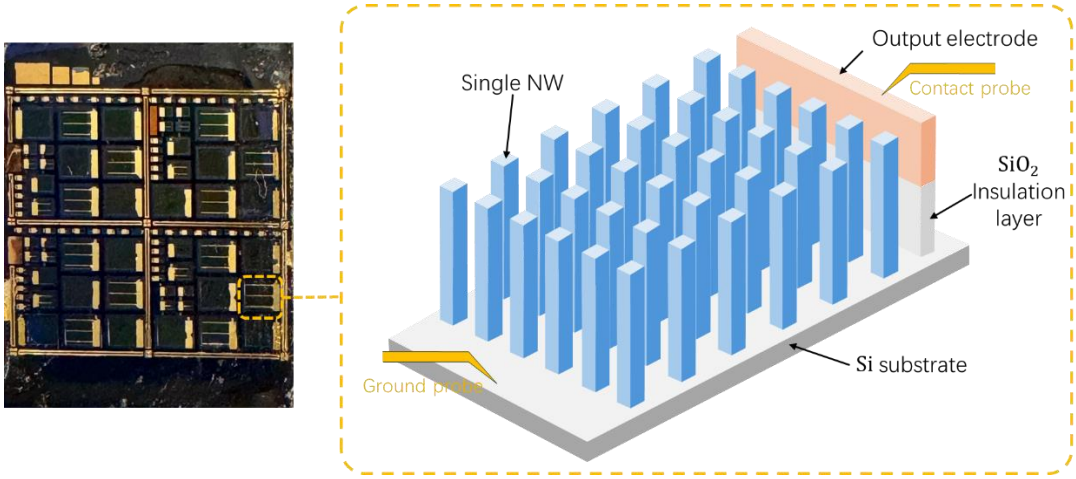

Figure 3.7. *Optical photo of the nanowire device chip (left) and a schematic diagram of the selected nanowire array used for measurement (right). In the diagram, the nanowire array is located between the ground probe in contact with the Si substrate and the contact probe touching the output electrode. The array is covered with SiO_2 insulation and a DASA molecular layer, which can adjust the channel current under illumination.*

(2) Measurement conditions and physical mechanism

Electrical measurements are performed under the condition of zero bias (0 V) to exclude carrier drift caused by external electric fields. Before conducting the photoelectric gate control experiments, first use the scanning function of the SourceMeter to record the I–V characteristics of the nanowire array to verify its electrical continuity. The measured I–V curve confirms that all nanowires are in good contact and the device shows the expected conductive behavior of the nanowire array. Performing this verification step ensures that the subsequent zero-bias photocurrent measurements truly reflects the inherent photo-modulation, not the contact artifact.

Zero-bias operation is also commonly used in the characterization of photovoltaic or solar-cell-type devices, because it allows the extraction of photogenerated carrier behavior without introducing externally induced drift currents. For the present nanowire devices, this condition ensures that the observed current variations originate purely from light-induced potential modulation and carrier density changes.

The G2V light source illuminates the entire device area with the same intensity as used in the optical tests. When DASA molecules are switched from the closed form to the open form under illumination, their dipole moments change, generating local electric-field variations on the nanowire surface. This process can be regarded as the formation of an equivalent gate voltage (ΔV_g) that modulates the band structure and carrier concentration of the channel, thereby altering the overall conductivity of the device. When the light is turned off, the molecules relax back to their thermal-equilibrium configuration, ΔV_g disappeared, and the current returns to its initial value. This mechanism corresponds to a typical photogating effect, in which the dye layer indirectly controls the channel

conductivity through photo-dipole modulation.

To distinguish the role of the two dyes, we use the G2V LED module for multi-channel illumination. Each LED channel is independently controlled in intensity: the 652 nm channel matched the main absorption peak of AP-048, while the 568 nm channel matched that of AP-066. Because the LEDs are broadband sources with partially overlapping spectra, some cross-bleaching may occur. During testing, the two channels are switched alternately at intervals of several tens of seconds to separate the responses of each dye. Before each measurement, the samples are kept in the dark long enough to ensure a fully recovered initial state.

In addition, to investigate the direction selectivity of the photo modulation, polarization dependent measurements are performed on single dye samples. A linear polarizer is placed between the G2V LED output and the sample, allowing illumination at two polarization orientations: 0° ($E \parallel NW$) and 90° ($E \perp NW$). When the electric field is parallel to the nanowire axis, the molecular absorption and the induced field effect are strongest; when it is perpendicular, the absorption is weaker and the corresponding current change is smaller. This polarization dependence confirms the existence of orientation selective electro-optical coupling at the DASA–nanowire interface and provides an experimental basis for the anisotropy analysis discussed in the following results chapter.

Chapter 4 – Results and Discussion

This chapter presents the main experimental results of the DASA–nanowire hybrid devices. Based on the concepts introduced in Chapter 2 and the methods described in Chapter 3, we first examine the optical response of the DASA–PAMS films and their reversible switching behaviour. We then analyse how this molecular switching influences the electrical conductance of the nanowire devices under illumination. The time-dependent signals are fitted using simple kinetic models to extract characteristic bleaching and recovery times. Finally, the experimental observations are discussed in relation to the molecular properties, the polymer environment, and the nanowire optoelectronic behaviour.

4.1 Sample Preparation Optimization and Optical Baseline

Before conducting the photochromic and electrical response measurements, it was essential to ensure that the preparation process of the DASA thin films produced stable and reproducible optical characteristics. The optical absorption of DASA molecules in their closed form is highly sensitive to molecular packing and aggregation. Residual solvent and film morphology can therefore strongly affect the intensity and shape of the absorption peaks, as well as the overall reproducibility of the measurements.

In this study, AP-066 was chosen as a representative dye. It was dissolved in either DCM or toluene and mixed with PAMS as the host polymer. Different drop-casting approaches were compared to establish a reliable and reproducible preparation procedure for optical and photoelectrical measurements.

Three types of samples were prepared on the sapphire substrates:
(1) Unheated drop-casting sample: drop the dye solution on the center of the substrate and dry naturally at room temperature.
(2) Heated drop-casting sample: after deposition, heat the sample at $35\ °C$ for 5 min to promote solvent evaporation (details in Section 3.1.2).
(3) Tilted drop-casting sample: during the deposition process, the substrate is slightly inclined, so that the dye solution can flow and form a thin, gradient layer without additional heating.

Figure 4.1 shows the absorption spectra of these three samples. At $568\ nm$, the heated sample exhibits the most obvious and clear absorption peak, indicating that the molecular order is improved and the film thickness is more uniform. In contrast, the unheated sample shows a broader and lower absorption band, indicating the existence of local aggregation and uneven accumulation. The overall absorption of the tilted sample is the weakest, which is due to its thinner film and lower concentration of effective dye in the optical path. These results confirm that moderate post-deposition heating can effectively improve the uniformity and optical density of the film, providing a stable baseline for subsequent experiments.

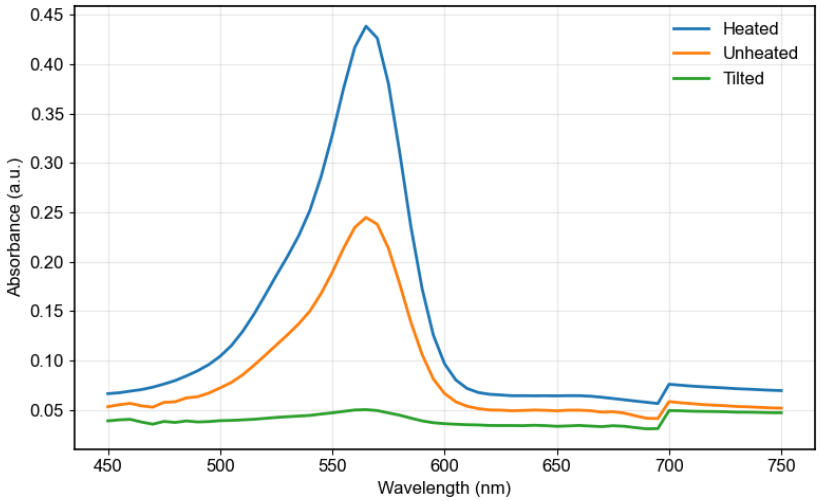

Figure 4.1. *The absorption spectra of AP-066 films on sapphire substrates prepared under different conditions. Blue: heated; orange: unheated; green: tilted. The heated sample shows the strongest and most symmetrical absorption peak at 568 nm, while the tilted sample shows the weakest absorption.*

These differences show that low-temperature heating can effectively promote solvent evaporation, improve molecular distribution and film density, thus enhancing uniformity and signal strength. Therefore, the procedure of drop-casting followed by heating at 35 $°C$ for 5 minutes was chosen as the standard method for all samples in this work, including both sapphire based and nanowire based hybrid devices. This protocol produced the most uniform films and yielded consistent optical responses, forming a reliable foundation for later studies on photobleaching, thermal recovery kinetics, multi-wavelength channel control, and electrical characterization.

4.2 Photodynamic Behavior of AP-048 and AP-066

To systematically compare the optical response characteristics of two generations of DASA dyes under different illumination wavelengths, this section focuses on AP-048 (the red-absorbing dye, hereafter noted as D_R) and AP-066 (the green-absorbing dye, D_G). Both belong to the Donor–Acceptor Stenhouse Adduct (DASA) family and can undergo reversible open-ring/closed-ring conversion under visible light. However, their donor–acceptor combinations and conjugation lengths differ significantly. D_R has a stronger acceptor and a longer conjugation path, giving a main absorption peak near 652 nm, while D_G has a shorter conjugation and a more localized acceptor, and the absorption peak is close to 568 nm. These structural differences indicate that they have different reaction kinetics and steady-state behaviors.

Illumination is provided by two LED modules installed in the G2V solar simulator, which match the corresponding absorption bands: LED-G (459–568 nm) and LED-R (633–711 nm). All films were prepared using the same heated drop-casting method (see §3.2.3) and measured in a closed Bentham spectroscopic system under constant light intensity. Transmission spectra were automatically recorded at fixed time intervals.

As seen in **Figure 4.2**, D_R shows a rapid decrease in transmission under red illumination (LED-R)

and quickly reaches a stable photostationary state, while almost no change occurs under green light. In contrast, D_G exhibits a gradual and continuous change under LED-G illumination, reflecting a slower but well-resolved conversion process, and shows negligible response under red light. Thus, both dyes possess strong spectral selectivity, but their reaction speeds differ significantly.

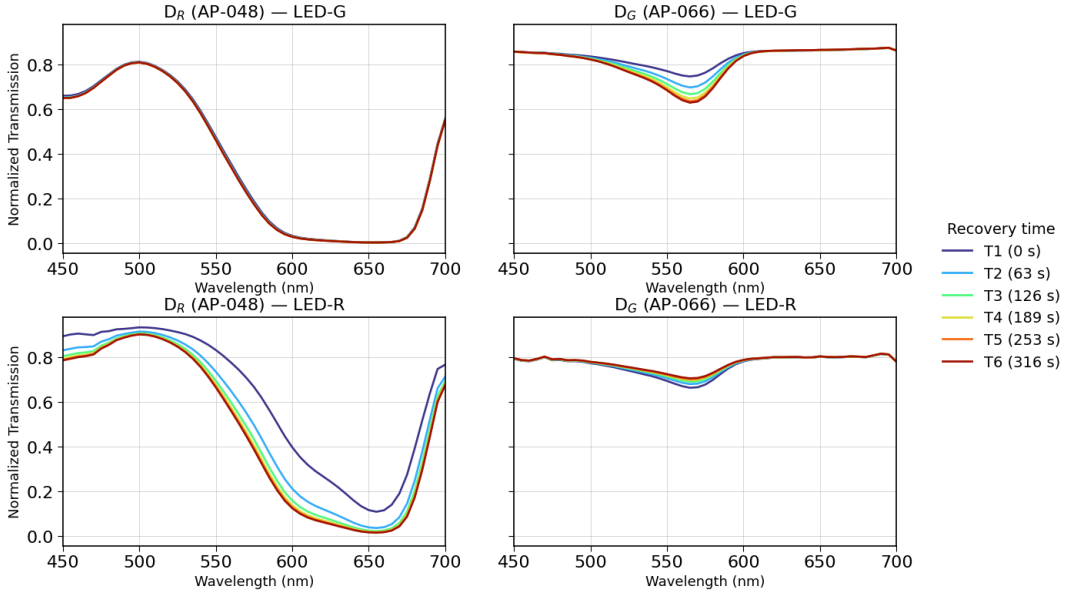

Figure 4.2. *Time-resolved transmission spectra of D_R (AP-048) and D_G (AP-066) thin films under different illumination conditions. Top: LED-G (459–568 nm); bottom: LED-R (633–711 nm). Left: D_R; right: D_G. Each curve (T1–T6) corresponds to a spectrum recorded at a different recovery time after the illumination was switched off, capturing the thermal back-reaction kinetics of the dyes. Both dyes show clear wavelength selectivity but different kinetic behavior.*

Under constant illumination, a DASA ensemble forms a dynamic equilibrium between light-induced conversion and thermally driven back-reaction. Over time, the molecular population shifts from the closed form toward a certain proportion of the open form, eventually reaching a steady state. The rate at which this equilibrium is established depends on two competing factors: the photo-induced conversion rate (the efficiency of structural rearrangement after photon absorption) and the thermal back reaction rate (the rate of spontaneous recovery). Light intensity, activation barriers, and donor–acceptor coupling strength all influence this balance. When both forward and backward processes are fast, equilibrium is reached rapidly; when one is slow, the approach to steady state is gradual.

The rapid convergence of D_R spectra in Figure 4.2 indicates a fast equilibrium, while the step-wise evolution of D_G implies a slower approach. These represent two kinetic extremes: D_R corresponds to a “fast-switching but short-lived” type, whereas D_G represents a “slow-responding but stable” type.

The difference likely originates from the molecular structure and the electronic properties of the ground state. According to the theoretical analysis in **Chapter 2** (see Eq. (6) and Eq. (8)), the photoinduced process can be understood as the combination of two opposing reactions: light-driven bleaching and thermally activated back reaction. The competition between these two processes determines the temporal response and the proportion of the steady photo-stationary state. Philip et

al.[27] further demonstrated that the thermal recovery rate k_{back} of DASA is closely related to the degree of ground state polarization. Stronger donor–acceptor charge separation leads to higher molecular polarization, a lower energy barrier for ring closing, and therefore a faster recovery rate. Theoretical calculations indicate that a more negative bond length alternation (BLA) and a larger solvatochromic red shift correspond to stronger polarization and higher k_{back}. The experimental results in this study are consistent with this rule: D_R, having stronger donor–acceptor interaction and a longer conjugated backbone, shows higher polarization and lower activation barrier, resulting in faster photoresponse and quicker establishment of steady state. In contrast, D_G has weaker polarization and a more symmetric structure, giving a higher barrier and a slower but more stable photoresponse. This correlation between molecular structure and kinetic behavior represents an important design principle for DASA materials.

Apart from the intrinsic molecular structure, the external environment can also influence the reaction rate. Abbey et al. reported that the recovery of DASA molecules proceeds faster in non-polar polymer matrices than in polar PMMA, suggesting that a polar environment stabilizes the closed form and slows the back reaction. In addition, higher concentrations can enhance intermolecular interactions and overall polarization, also leading to slightly faster recovery. Since the preparation conditions of the samples (concentration, thickness, and environment) in this study are similar, the differences observed are mainly attributed to the internal molecular structure. It is worth noting that under LED-R illumination, the spectrum of D_R almost immediately overlaps after excitation, indicating that its photostationary state is established very quickly. This also means that D_R molecules may have denser accumulation or stronger local interactions, thus achieving more efficient energy transfer and non-radiative relaxation. In contrast, the spectral evolution of D_G is relatively slow, suggests a looser molecular arrangement or weaker interaction with the substrate, leading to more independent molecular behavior.

In summary, D_R and D_G represent two typical photo-responsive patterns of DASA molecules. D_R shows stronger absorption, faster response, quicker recovery, and rapid establishment of dynamic equilibrium. On the other hand, the absorption efficiency of D_G is relatively low, its bleaching amplitude is small, and the change is slower at the same concentration, but provides higher stability and better spectral control. This comparison reveals the direct connection between donor–acceptor electronic properties and kinetic response, and explains the distinct application trends of DASAs in different structures. D_R molecules are more suitable for fast-response and rewritable optical modulation systems, such as optical logic devices or optical switching sensors, while D_G molecules are preferred for stable, progressive, and long-life photo=responsive systems. The consistency of experimental observations and theoretical models indicates that variations in molecular structure and electronic distribution may play an important role in shaping the kinetic behavior, which provides a solid foundation for future multi-wavelength optical control and hybrid system design.

4.3 Optical Response and Cooperative Effect in Mixed Samples

To explore the interaction and response behavior of D_R and D_G coexisting in the same film, we studied mixed samples containing both dyes. Compared with single-dye films, the mixed system may show two independent absorption centers or new kinetic features due to energy transfer or

uneven light distribution. By analyzing the evolution of transmission spectra at different illumination wavelengths, the coupling relationship between absorption efficiency, energy distribution and photochemical dynamics can be clarified.

Such research is crucial for the development of reversible photochromic materials with different responses at different wavelengths. A single dye typically reacts only to a narrow wavelength range, whereas properly designed mixtures can extend sensitivity and enable multiband optical modulation, useful for multichannel data storage, spectral display, and adaptive optical filters. Here, a 1:1 mixture was first examined as a baseline reference for later optimization.

4.3.1 Spectral Characteristics and Unbalanced Response

Figure 4.3 shows the normalized transmission spectra of D_R, D_G, and the thin film formed by mixing them in a 1:1 volume ratio under continuous illumination over time. The top two figures correspond to the reference results for single dyes, while the bottom figure shows the performance of the mixed sample. The red dashed lines indicate the two characteristic absorption bands at approximately 568 nm and 652 nm (see **Figure 4.3**).

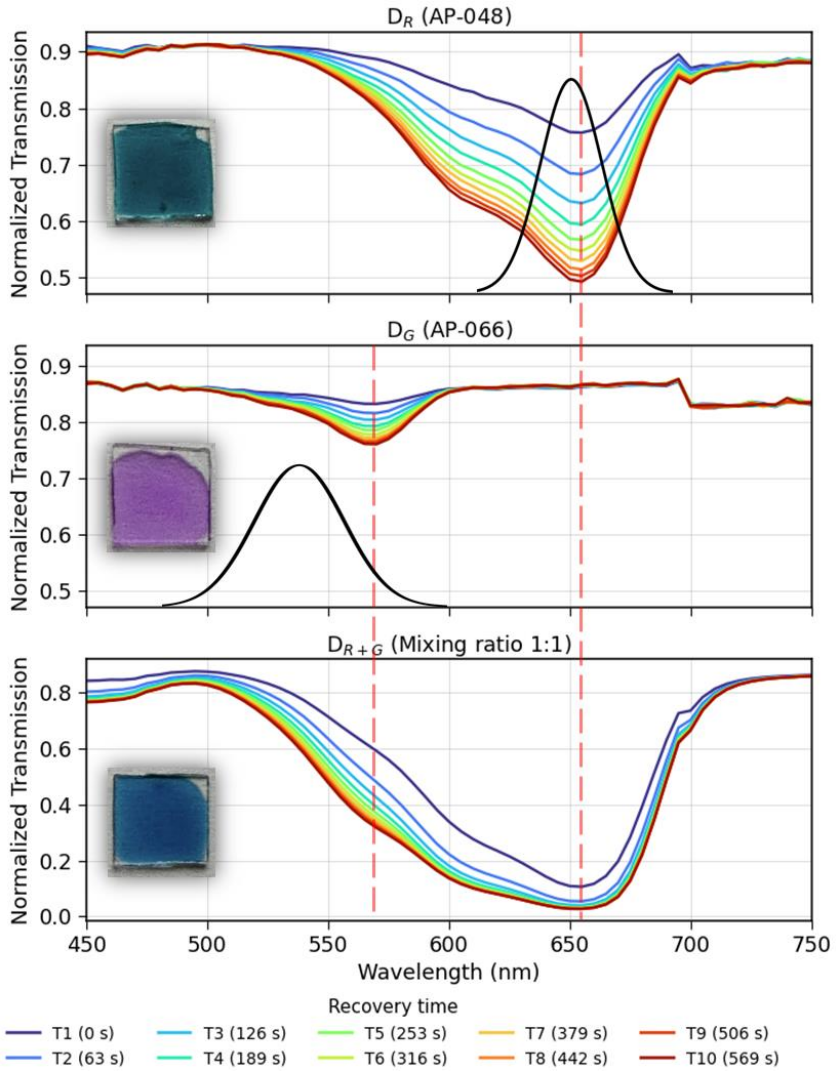

Figure 4.3. *Time-resolved transmission spectra of D_R (AP-048), D_G (AP-066), and their 1:1 mixed film under continuous illumination. Red dashed lines mark the characteristic absorption bands at 568 nm*

and 652 nm. The black curves represent the emission spectra of LED-R (top) and LED-G (middle). The strong spectral overlap in the red region leads to a faster and stronger response of D_R, while the excitation of D_G is relatively weaker due to its poorer overlap with the absorption band. The mixed sample retains two absorption characteristics, but the overall response is still dominated by the red region, showing unbalanced photobleaching behavior. The inset shows the macroscopic appearance of the corresponding sample.

In single dye samples, D_R shows obvious bleaching around 652 nm, while D_G shows weaker absorption at 568 nm and gradually decays. The mixed film retains these two characteristics, confirming that the two molecules in the composite are still photoactive and reversible. However, the amplitude of spectral change at 652 nm is significantly greater than at 568 nm, indicating that the overall response is dominated by the red absorbing component.

This imbalance mainly stems from two cooperative factors. First, there are significant differences in the overlap of illumination and absorption spectrum of different dyes. As shown in Figure 4.3, LED-R emission overlaps almost perfectly with the absorption band of D_R, providing higher effective excitation intensity, while the green illumination overlaps only partially with D_G. Since the bleaching rate is directly proportional to the absorbed photon flux, D_R undergoes stronger excitation and consequently faster photobleaching.

Second, the intrinsic kinetic difference between the two dyes further amplifies this contrast. D_R converts and recovers more rapidly than D_G, producing a two-stage temporal response when both coexist. In the mixed film, the rapid bleaching of D_R dominates the early dynamics, while the slower evolution of D_G leads to a more gradual change in the green-region signal. Importantly, D_G already exhibits a weaker response in its single-dye film, and this inherent weakness is preserved in the mixed system.

In addition to these primary factors, a subtle inner-filter-like effect (IFE) may also contribute to the observed behavior. The absorption tail of D_R extends toward shorter wavelengths up to ~570 nm, meaning that in regions where D_R is locally more concentrated, part of the incoming green light may be re-absorbed before reaching D_G. Such local light-field attenuation could slightly reduce the effective excitation intensity experienced by D_G.

Although our measurements do not allow a quantitative separation between additive absorption and possible redistribution effects, the mixed-film spectra qualitatively resemble the superposition of the two single-dye responses, with a small additional suppression in the green region. Similar "locally absorption-dominated" phenomena have been reported in other mixed-dye thin films[64][65], suggesting that IFE may serve as a secondary contribution, but the predominant reason for the weaker D_G signal remains its intrinsically lower green-region response.

Overall, although the 1:1 mixture maintains dual absorption centers, its photochemical energy distribution and kinetics remain unbalanced, with D_R dominating the overall response. Such imbalance reduces color uniformity and indicates that equal proportions do not yield cooperative excitation. To achieve balanced multiwavelength response, the composition must be further adjusted

or illuminated with spectrally matched light sources.

4.3.2 Comparison of Different Mixing Ratios and Optimal Response

To optimize the balance between the photo-responses of D_R (AP-048) and D_G (AP-066) in single-layer films, this section investigates the dynamic evolution of transmission spectra at different mixing ratios. Previous experiments showed that in the 1:1 mixed system, absorption in the red region (D_R) strongly dominated, while the response in the green region (D_G) was insufficient. To reduce the excessive absorption of D_R and enhance the excitation contribution of D_G in the shorter wavelength range, the D_G content was gradually increased (which can also be viewed as a relative dilution of D_R concentration). Five mixed samples were prepared with D_R: D_G ratios of 1:1, 1:10, 1:20, 1:30, and 1:40. Under identical illumination conditions, time resolved transmission measurements were performed to systematically evaluate the photobleaching and recovery dynamics across these different compositions.

Figure 4.4 shows the time evolution of the normalized transmission spectra for samples with different mixing ratios under continuous illumination. The spectral dynamics at the two main absorption bands (around 568 nm and 652 nm) vary significantly among the samples.

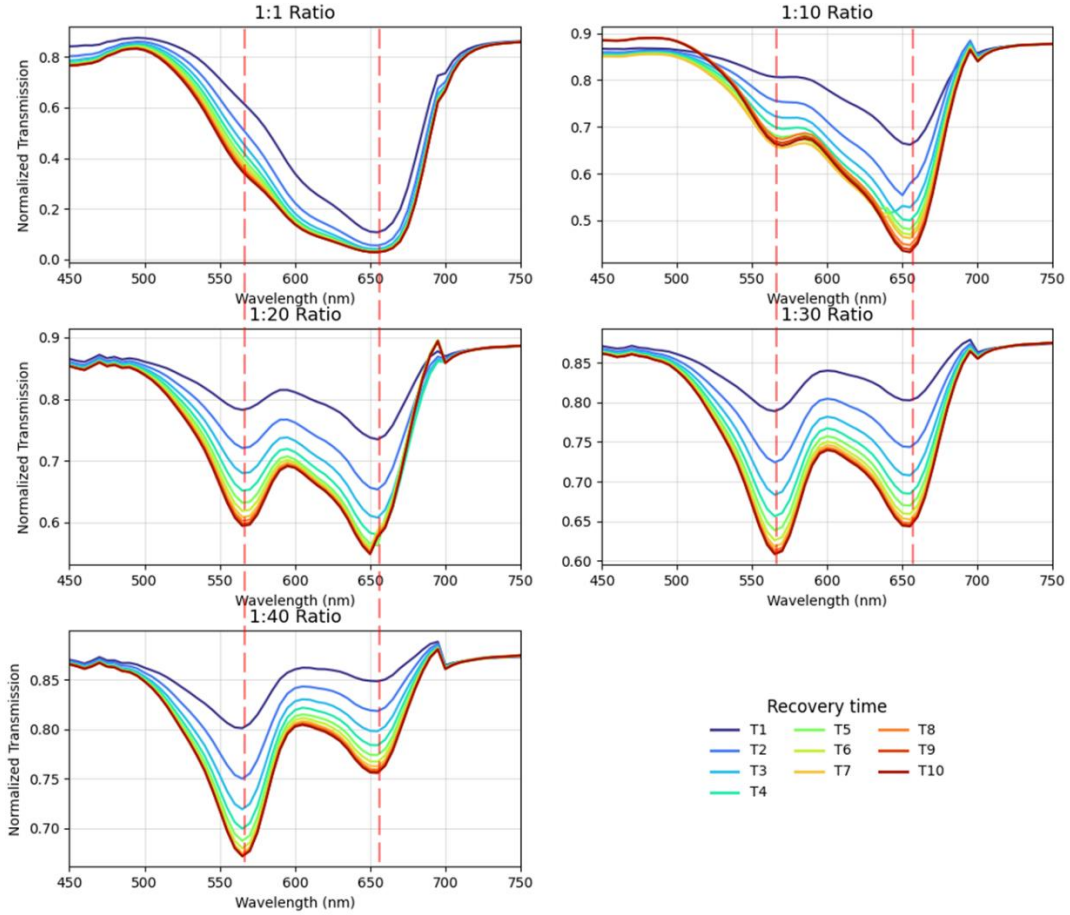

Figure 4.4. *Time-resolved normalized transmission spectra of mixed films with different D_R: D_G ratios (1:1, 1:10, 1:20, 1:30, 1:40) under continuous illumination. The red dashed lines mark the characteristic wavelengths at 568 nm and 652 nm, corresponding to the primary absorption features of D_G and D_R, respectively.*

For the 1:1 sample, bleaching in the red region is dominant while the green region responds more weakly, and the uneven spacing between spectral lines indicates that the system is still mainly governed by D_R, with the photoisomerization efficiency of D_G being limited. When the ratio increases to 1:10, although the D_G content rises, the spectra still show faster variation in the red region and slower changes in the green region. The bleaching dynamics exhibit a clear two-stage behavior: an initial rapid response dominated by D_R, followed by a slower recovery phase associated with D_G. The modulation amplitude difference between the two peaks is still large, suggesting that the energy distribution has not reached equilibrium.

When the ratio is further adjusted to 1:20 and 1:30, the spacing between the spectral lines becomes more uniform, and the two absorption bands show synchronous reduction and saturation under illumination. This characteristic indicates that the bleaching and recovery rates of D_R and D_G have become comparable, and the energy transfer and light field distribution in the film are close to equilibrium. The transmittance changes at 568 nm and 652 nm are similar, showing a regular and nearly linear increase over time, and there is no obvious separation between fast response and slow response, indicating that there is a good kinetic matching between the two molecular species. In addition, the smoothness and symmetry of the spectral profiles suggest that the quality of the film is stable and the photoisomerization process is still reversible.

However, in the sample at 1:30 ratio, although two absorption bands remain visible, the overall modulation amplitude slightly decreases, implying that the signal begins to weaken as the total dye concentration of the dye decreases. For the 1:40 sample, absorption in the green region clearly dominates, and the irregular spacing between the spectral lines indicates that the excessive D_G content causes the optical response of the system to shift toward shorter wavelengths, reducing the contribution of D_R. The overall spectral variation is relatively small, showing that the excessive dilution of D_R significantly reduces the modulation depth of the system.

In summary, the spectral dynamics of samples with different mixing ratios reveal the competition between light absorption, energy distribution and photochemical reaction rate in the system. The mixed films with ratios of 1:20 and 1:30 exhibit clear and well-balanced bleaching dynamics at both absorption centers, indicating that there is an effective cooperative excitation between D_R and D_G. Among them, the 1:20 sample has the best performance, its absorption peaks are symmetrical, spectral changes are uniform, and the photobleaching and recovery processes are well synchronized. Compared with the 1:30 sample, the 1:20 film shows larger transmittance changes at both absorption bands and higher signal contrast, providing clearer dynamic characteristics for quantitative analysis and device-level research. Based on these considerations, an on-chip optical experiment is then conducted with the mixed ratio of D_R: D_G = 1:20 to further investigate its dynamic optical behavior in microstructured environments.

4.3.3 Optical Stability and Reproducibility

To evaluate the stability and repeatability of the mixed films under repeated illumination, we used time-resolved transmission spectroscopy to measure two representative components, D_R (AP-048): D_G (AP-066) = 1:1 and 1:20 twice. In the two measurements, the illumination spectrum, light intensity, and scanning procedure were consistent. Between the two runs, the samples were stored

in the dark and confirmed to have returned to their unbleached state before retesting. In the following analysis, the curve with the highest transmission within each time series is regarded as the most bleached state, while the lowest transmission corresponds to the unbleached state. The difference between the two indicates the dynamic modulation range achieved during that cycle.

Figure 4.5 shows the spectral evolution of the two mixing ratios during both measurements. It can be seen that the overall spectral shapes and peak positions remain nearly identical, but the absolute transmission increases and the absorption depth decreases in the second run. This observation suggests that a fraction of molecules underwent irreversible changes during the first illumination cycle. Some molecules may have been locked in their open ring or non-absorbing configurations, or experienced irreversible chemical or conformational transformations. As a result, these molecules no longer contribute to absorption in the "unbleached" state of the second measurement, leading to a higher baseline transmission. At the same time, since the fraction of reversibly switching molecules decreases, the apparent bleaching and recovery processes become faster, but the overall modulation amplitude is reduced.

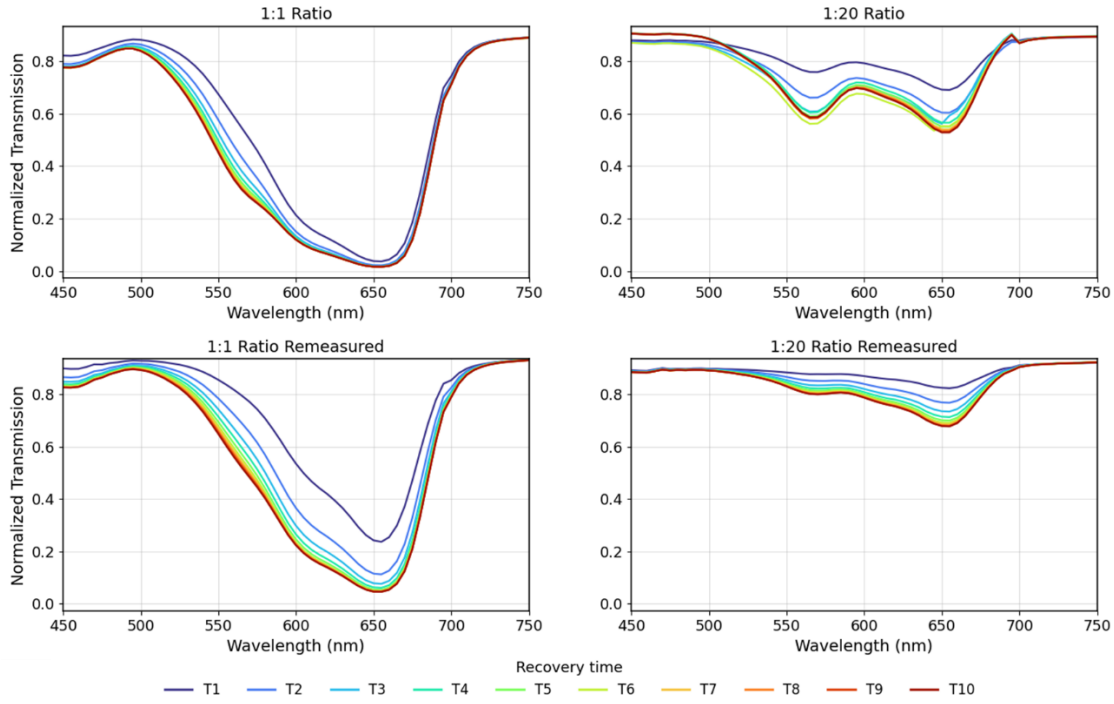

Figure 4.5. *Time-resolved normalized transmission of mixed films with D_R: D_G = 1:1 and 1:20 under identical illumination. Top: first run; bottom: second run after dark recovery. In each panel, the highest transmission trace represents the most bleached state; the lowest corresponds to the unbleached end.*

Both compositions show the same overall trend, but the difference lies in the amplitude and distribution of the response. In the 1:1 sample, the two spectral sets almost overlap, with only a slight reduction in dynamic range. This suggests that the proportion of irreversible components is relatively low and that the spectral features remain well preserved. However, its intrinsic modulation depth is smaller, meaning that without increasing the light dose, the achievable optical contrast is limited. In contrast, the 1:20 sample exhibits a much stronger change, in the second measurement, both absorption bands become shallower, especially the D_G related band near 568 nm, where absorption is almost flattened. This indicates that, at this ratio, the first illumination more easily

generates a “permanently transparent” fraction of D_G molecules, resulting in a more noticeable baseline increase, a smaller dynamic range, and a faster convergence of the time sequence toward higher transmission during the second test. In other words, the 1:20 film shows stronger activity and clearer dual peak features in the first cycle, but its D_G-related features become noticeably weaker in the second cycle, suggesting a larger irreversible component or a gradual loss of optical contrast rather than a fully reversible modulation.

This behavior can be explained by several factors. First, the absorption ranges of the two dyes do not perfectly match the emission spectra of the light source. During illumination, one dye may absorb more energy than the other. For the component present at a higher ratio, the absorbed energy during the first exposure may reach the threshold that triggers irreversible bleaching, leaving behind a portion of molecules that no longer respond. Second, after strong illumination, the micromorphology of the film may be slightly reorganized. For example, changes in molecular accumulation, aggregation, or local polarity may cause certain molecules to remain open. While this does not shift the position of the absorption peak, it will reduce the number of particles that can be used for reversibility, leading to faster but smaller changes in subsequent measurements. Third, the strong initial bleaching will alter the internal light distribution: once the top layer becomes more transparent, the light will penetrate the film deeper, accelerating the bleaching of the remaining molecules while reducing the overall absorbance. Slight fluctuations in instruments or illumination could also have an impact, but this effect can be ruled out because the wavelength of the absorption peak remains almost unchanged. Therefore, the most reasonable explanation is that the first illumination leaves a small fraction of permanently bleached molecules, while the remaining active molecules will react in a narrow range.

From a methodological point of view, these results indicate that the optical response of mixed DASA films is not completely reversible or irreversible; on the contrary, these two processes coexist and compete under given illumination doses, ratios, and film morphologies. The 1:1 film has better repeatability and more stable spectral shape, but the modulation depth is smaller. The 1:20 film exhibits stronger initial bleaching and clearer double peak contrast, but its D_G channel decays faster in repeated cycles, which means that a strong first response does not guarantee long-term durability.

Experiments show that to improve the stability and repeatability of mixed DASA films, it is necessary to avoid excessive light to avoid large-scale molecular damage. Lowering the illumination power or extending the recovery time between exposures can restore more molecules to a closed state, thus reducing irreversible bleaching. During manufaction, consistent control of film thickness and annealing conditions is also crucial to minimize morphology induced changes. For ratio design, fine-tuning between 1:20 and 1:30 (for example, 1:25) may help to achieve a better balance between response amplitude and repeatability. Future research could include repeated measurements at the same location and power stability checks of the light sources to further vilify their long-term performance.

In a word, both mixed ratios show coexistence of reversible and irreversible components under repeated illumination: the spectral peak positions remain stable while the baseline shifts upward, and the time sequence converges faster with a smaller dynamic range. The 1:1 sample demonstrates

slightly better stability and retention, whereas the 1:20 sample provides a stronger initial response but faster degradation in the D_G channel. Overall, careful control of illumination intensity, film fabrication, and dye ratio will be key to improving repeatability and operational lifetime.

4.4 Dual Wavelength Synaptic Channels on Nanowire Arrays

In the previous sections, we confirmed that D_R (AP-048), D_G (AP-066), and their mixtures all exhibit good reversible photobleaching behavior when deposited on flat sapphire substrates. To further explore their cooperative behavior in a functional device structure, in this section the mixed film was drop-cast onto a InP nanowire array (NWA). Using dual wavelength pulsed illumination, we achieved multichannel optical signal writing and reading based on the distinct responses of the two dyes.

4.4.1 Experimental Concept and Channel Definition

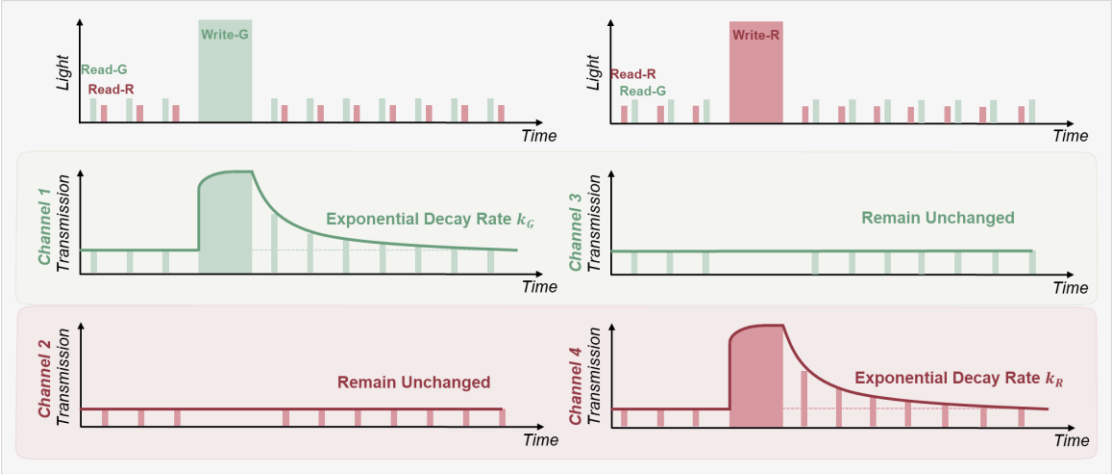

Figure 4.6. *Schematic illustration of the four communication channels under dual-wavelength pulsed illumination. Write/Read-G → LED-G (matching AP-066); Write/Read-R → LED-R (matching AP-048). Each write pulse induces bleaching in its corresponding dye, followed by exponential recovery detected by the read pulses.*

Figure 4.6 shows a schematic diagram of the experimental setup. The system consists of two independently controlled light sources: LED-G corresponds to the absorption range of D_G (approximately 459–568 nm), and LED-R corresponds to that of D_R (approximately 633–711 nm). The illumination sequence alternates between weak read (Read) pulses and stronger write (Write) pulses. The first few Read pulses establish the baseline signal, after which a Write pulse causes photobleaching, followed by the same Read sequence to monitor the recovery process. When using LED-G for writing, D_G molecules are excited and bleached, while D_R is not expected to be affected; conversely, under LED-R illumination, bleaching mainly occurs in the D_R channel. Based on this configuration, four optical communication channels can be defined:

Channel	Write Source	Read Source	Main Responsive Dye	Behavior
1	Write-G	Read-G	D_G	Exponential bleaching and recovery
2	Write-G	Read-R	D_R	Nearly unchanged
3	Write-R	Read-G	D_G	Nearly unchanged
4	Write-R	Read-R	D_R	Exponential bleaching and recovery

By comparing these four channels, the wavelength selectivity and independence of both dyes can be directly evaluated, providing an experimental basis for multi-channel optical data storage.

4.4.2 Optimization and Mechanistic Validation of Wavelength-Selective Channels

This study optimizes the illumination intensities of both Write and Read pulses through experiments. The optimization process follows two main principles:

• The Read pulse intensity should be high enough to produce a stable photocurrent but not strong enough to cause photobleaching.

• The Write pulse intensity should effectively induce molecular bleaching, while avoiding the photovoltaic response of the dominant signal of the nanowire array or causing permanent damage.

Based on the above standards, the final parameters are selected as follows:

• Write-G and Write-R: approximately 0.3 $mW\ cm^{-2}$ (corresponding to an LED power setting of 500).

• Read-G: approximately 0.02 $mW\ cm^{-2}$ (power setting 35); Read-R: approximately 0.015 $mW\ cm^{-2}$ (power setting 30).

• The interval between Read-G and Read-R pulses is 5 seconds, and the interval between consecutive Read sequences is 10 seconds.

These optimization settings ensure signal stability and no obvious cumulative bleaching during repeated tests. For the detailed verification process and power-dependent measurements, please refer to Appendix B: *Illumination Optimization Tests*.

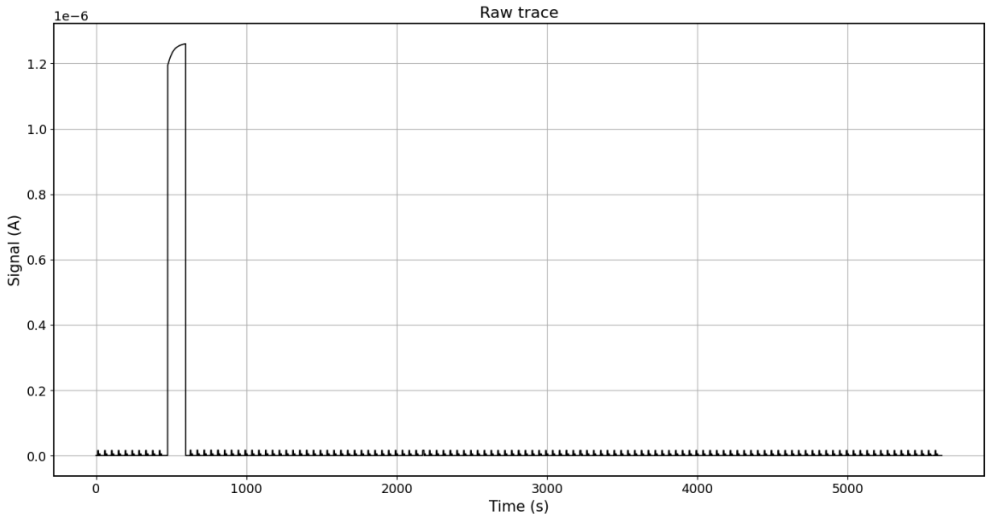

Figure 4.7. *Raw current trace recorded from the nanowire array during the dual-wavelength*

illumination sequence. The strong write pulse causes the transient photocurrent to rise, followed by periodic read-pulse responses showing the behavior of gradual recovery .

Figure 4.7 shows the raw current trace of the device during a complete illumination cycle. When a Write pulse is applied, the current rises sharply and reaches a saturation plateau, which corresponds to the transient process of dye molecules being excited into the open form, leading to absorption enhancement and carrier increase. To further analyze the recovery characteristics of the optical response, all Read pulse segments are extracted from the full signal and processed individually. Specifically, the average of multiple sampling points is carried out on the plateau region of each Read pulse to obtain the steady-state current at that moment, minimizing the impact of transient noise. Then these averages are arranged in chronological order to form a Read sequence curve that changes over time, which clearly reflects the bleaching and recovery behavior of the device.

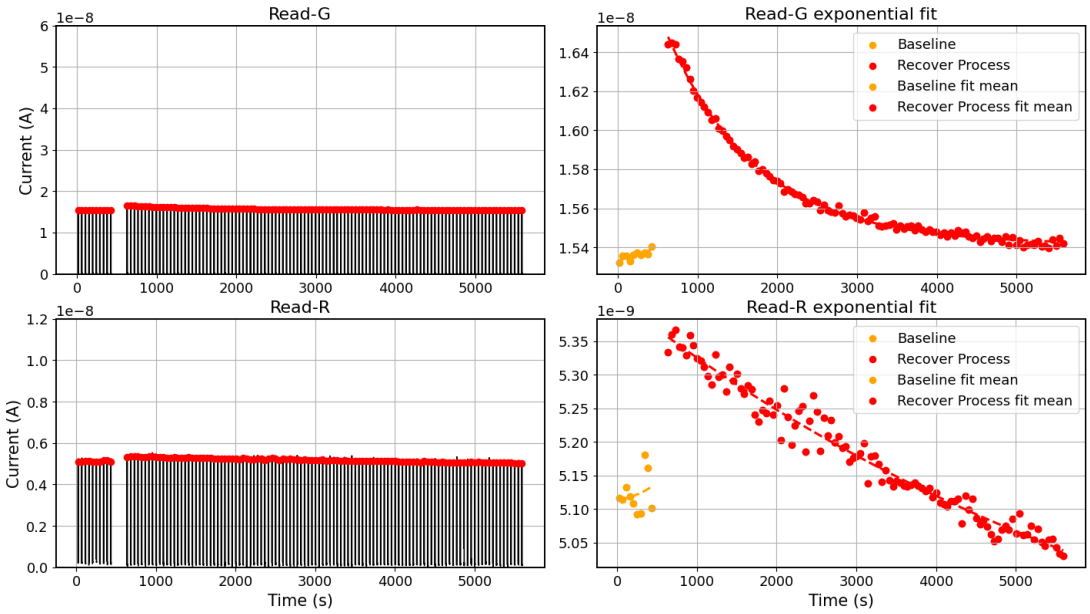

Figure 4.8. *Read-pulse responses and exponential fitting under Write-G illumination. After a single green light write pulse, the Read-G and Read-R signals are recorded. The Read-G channel exhibits a clear exponential decay, corresponding to the reversible bleaching of D_G, while the Read-R channel shows only a weak, nearly linear change, indicating that the crosstalk from the red region is extremely small.*

As shown in **Figure 4.8**, the first few Read pulses (marked in yellow) correspond to the baseline signal before bleaching, while the subsequent pulses (marked in red) gradually decrease, showing a typical exponential recovery trend. The upper plot displays fitting results in exponential coordinates, and the lower plot shows the same data in linear coordinates, so that the changes in recovery behavior over time can be clearly observed.

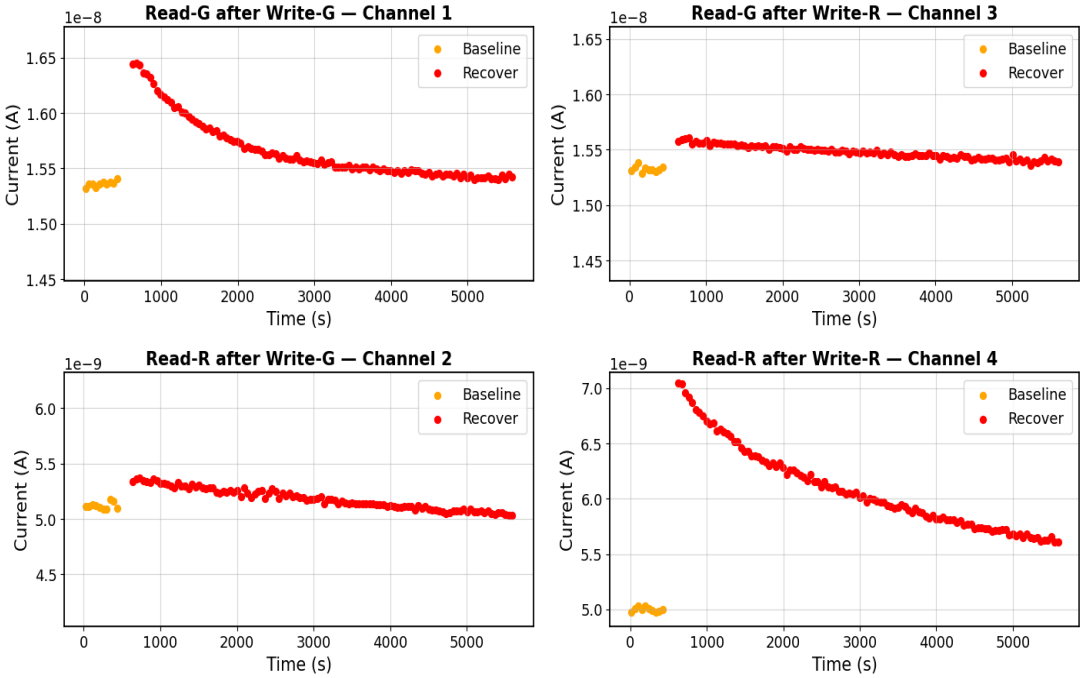

Figure 4.9. *Channel resolved read pulse responses under dual wavelength illumination. Each panel shows the averaged read pulse current and corresponding exponential fitting for the four communication channels: (Top left) Read-G after Write-G (Channel 1); (Bottom left) Read-R after Write-G (Channel 2); (Top right) Read-G after Write-R (Channel 3); (Bottom right) Read-R after Write-R (Channel 4). Directly illuminated channels (1 and 4) exhibit clear exponential decays associated with reversible bleaching, whereas indirectly affected channels (2 and 3) show only minor, nearly linear variations, indicating weak optical cross*-talk.

As shown in **Figure 4.9**, the left panel corresponds to the two channels obtained under Write-G excitation (Channels 1 and 2), while the right panel shows the results under Write-R excitation (Channels 3 and 4). Comparing all four channels, two distinct response types can be clearly identified: channels directly exposed to the writing light (Channels 1 and 4) exhibit typical exponential decay, whereas the non-illuminated channels (Channels 2 and 3) show nearly linear variations with only very small amplitude changes compared with the directly written channels.

For Channel 1 (Write-G → Read-G), the current rises rapidly after the write pulse and then follows a standard exponential recovery, and finally returns to almost the baseline level. This indicates that D_G molecules undergo a fully reversible photobleaching and recovery cycle, bringing the system back to its unbleached state. Channel 4 (Write-R → Read-R) also shows an exponential decay, but the signal does not completely return to the initial level, suggesting that part of the D_R molecules experience irreversible bleaching under red-light illumination. This partial irreversibility may result from deeper molecular embedding or stronger intermolecular interactions, leading to local structural degradation under high light intensity and leaving behind a “permanently transparent” fraction.

Together, these two behaviors form a “fast–slow channel” dynamic pair: Channel 1 responds quickly and recovers fully, making it suitable for short-term information writing, while Channel 4 recovers

more slowly and retains a residual signal, which can be useful for longer-term memory retention.

To further quantify the bleaching amplitude and dynamic differences between channels, the baseline and maximum bleaching currents were statistically compared (see Table 4.1). As shown, Channels 1 and 4 exhibit the most significant current variations, about 6–7% and 20–25%, respectively , whereas Channels 2 and 3 change by less than 5%, and their absolute variation is nearly an order of magnitude smaller than Channels 1 and 4. This confirms that the directly written channels exhibit clear electrical responses, while the indirect ones mainly reflect optical cross-talk or local scattering effects. Moreover, the slight decrease in Channel 2's final current suggests that, under enhanced local fields, red-light excitation may induce minor cooperative bleaching in the D_G absorption region. The incomplete recovery of Channel 4 is consistent with partial irreversible conversion of D_R molecules.

Table 4.1. *Estimated current change between baseline and maximum bleaching states for four channels*

Channel	Excitation–Read Relation	Baseline (A)	After Bleaching (A)	Change (%)	Response Type	Interpretation
1	Write-G → Read-G	~1.54×10^{-8}	~1.64×10^{-8}	+6–7%	Exponential	Fast, reversible bleaching
2	Write-G → Read-R	~5.1×10^{-9}	~5.3×10^{-9}	±3–4%	Linear	Weak cross-talk, minor offset
3	Write-R → Read-G	~1.53×10^{-8}	~1.55×10^{-8}	+1–2%	Linear	Nearly stable, minimal effect
4	Write-R → Read-R	~5.5×10^{-9}	~6.8×10^{-9}	+20–25%	Exponential	Strong bleaching, partial irreversibility

In contrast, Channels 2 and 3 are not directly exposed to the writing light, and their signals show nearly linear changes over time. The response of Channel 3 almost overlaps with the baseline, indicating that during the Write-R operation, the absorption band of D_G remains essentially unaffected. In Channel 2, the current is slightly lower than the baseline, suggesting that scattering or local field enhancement under red light illumination may extend into the D_G absorption region, producing a weak cooperative bleaching effect. Since this variation does not follow an exponential trend, it is more likely caused by spectral overlap, energy transfer, or background drift rather than an actual molecular reaction. In other words, direct writing leads to exponential decay, reflecting genuine photo-chemical kinetics, whereas indirect influence results in linear decay, representing pseudo responses dominated by optical cross-talk or noise accumulation. In the ideal scenario illustrated in **Fig. 4.6** this indirect channel would remain perfectly flat, yet in practice a weak residual signal appears, as seen in **Fig. 4.9**.

Overall, the results from all four channels clearly demonstrate that the mixed DASA film on the nanowire array can still achieve wavelength selective and independent optical responses. Both bleaching and recovery follow primarily single step transitions, consistent with the typical reversible photoswitching mechanism between closed and open forms. The D_G channel exhibits fast and fully reversible behavior, while the D_R channel is slower but more stable, though it shows partial

irreversibility. This dynamic characteristic of speed and speed complementary provides a natural advantage for the realization of multi-time scale optical memory. Compared with a flat substrate, the nanowire array enhances light absorption and signal amplitude, making the exponential recovery behavior more obvious. Although local scattering will produce slight crosstalk, the overall signal-to-noise ratio is still high, indicating that this structure has great potential for scalable multi-wavelength writing and neuromorphic optical synapse applications.

4.4.3 Long-Term Cyclic Stability

To evaluate long-term endurance, the Write–Read sequence was repeated six consecutive times on the same DASA–NWA device. According to **Section 4.3**, the typical relaxation constants for D_G and D_R are approximately $k_G \approx 8 \times 10^{-4}\, s^{-1}$ and $k_R \approx 1 \times 10^{-4}\, s^{-1}$, corresponding to recovery times of $10^2 - 10^4\, s$ (minutes to about one hour). Therefore, the interval between write pulses ($\approx 5000\, s\ or\ 1.4\, h$) was set long enough to ensure complete recovery to the unbleached state.

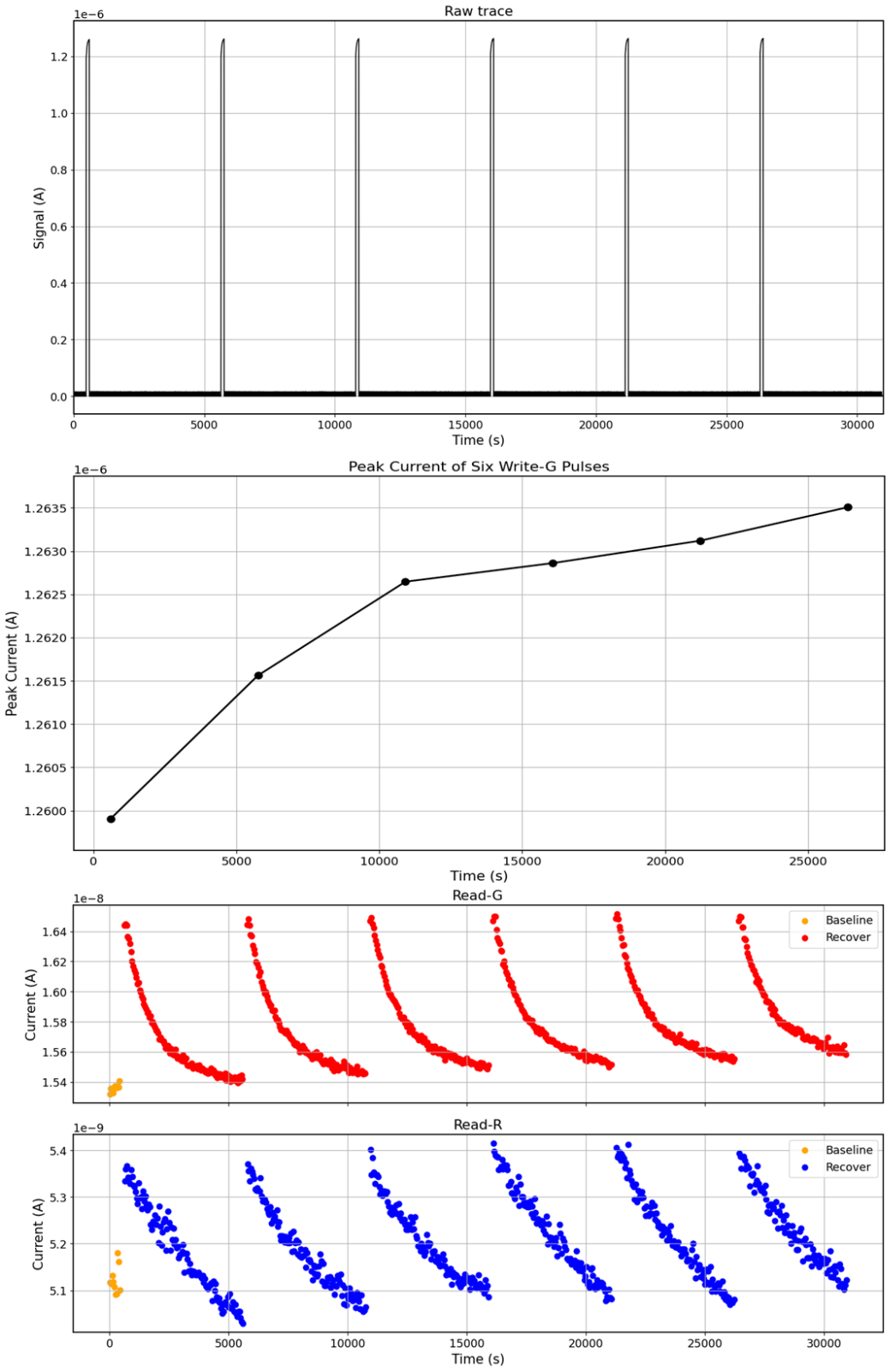

Figure 4.10. *Long-term cyclic response of the DASA–NWA device under repeated Write-G operations. (Top) Raw current trace recorded over six Write–Read cycles with* ~5000 *s intervals between write pulses. (Middle) Evolution of the peak current for each Write-G pulse, showing a gradual increase despite constant illumination intensity, suggesting incomplete recovery between*

cycles. (Bottom) Cycle resolved exponential fittings of Read-G (red) and Read-R (blue) responses, whose baseline currents shift upward with successive cycles, indicating cumulative irreversible bleaching or structural reorganization within the DASA–NWA film.

However, as shown in **Figure 4.10**, the measured peak current during the write process does not remain constant but gradually increases with each cycle. The peak value rises from about $1.260 \times 10^{-6}\,A$ in the first cycle to $1.264 \times 10^{-6}\,A$ in the sixth, and the corresponding cumulative increase is about 0.3–0.4%. This trend suggests that there is an accumulation of irreversible bleaching or structural reorganization inside the film. Some D_R or D_G molecules may remain permanently transparent after initial illuminations, resulting in a gradual increase in overall conductivity. Another possible explanation is that slight local heating during illumination causes mild morphology or accumulation changes in the film, creating more conductive pathways and enhancing the peak current in subsequent cycles.

When fitting each Read sequence with an exponential function, all channels show similar decay rates, but their baselines gradually shift upward as the number of cycles increases. This observation indicates that:
(1) the fundamental photochemical kinetics remain unchanged, still follows a one-step bleaching–recovery mechanism, and
(2) the proportion of reversible molecules gradually decreases, meaning the "reversible capacity" part of the system is consumed during continuous operation.

In other words, the DASA film on the nanowire array exhibits predictable and stable degradation behavior: the reaction kinetics remain steady, but the proportion of reversible species decreases over time.

Overall, this cyclic experiment clearly reveals the long-term optical evolution of the mixed DASA–NWA system. Although the accumulation of irreversible bleaching slightly shifts the signal amplitude, the periodicity and fitting reproducibility remain consistent, indicating that the system maintains a stable photoelectric response and can serve as a foundation for multicycle write–erase type optical memory devices.

4.5 Polarization Dependence and Mechanistic Validation of Multi-Channels

To investigate the spatial selectivity and light field sensitivity of the mixed DASA–NWA system in multi-channel optical responses, this section studies the photocurrent behavior of the device under different incident light polarization directions. Because the silicon nanowire array (NWA) exhibits anisotropic light scattering and local field enhancement, and the DASA molecules may become partially oriented during film formation, the photobleaching efficiency is expected to depend on the polarization angle.

As described in **Chapter 2**, the strength of light-matter interaction in an anisotropic nanostructure depends on the projection of the incident electric field onto the molecular transition dipole direction. Therefore, changing the polarization angle alters the effective absorption cross section and the

resulting photocurrent amplitude. When the polarization of the incoming light is aligned with the molecular dipole moment or the nanowire axis, the local field enhancement is maximized, leading to stronger light absorption and higher carrier generation efficiency. Conversely, when the polarization is perpendicular to the main orientation, the coupling efficiency decreases, resulting in weaker bleaching and smaller readout signals.

In the experiment, linearly polarized light was used while keeping the light intensity and pulse parameters constant. The polarization direction was adjusted by rotating a polarizer. The left panel represents the response when the polarization angle switches from 0° (first two pulses) to 90° (next two pulses), while the right panel shows the reverse sequence from 90° back to 0°. The corresponding raw current traces are shown in **Figure 4.11**.

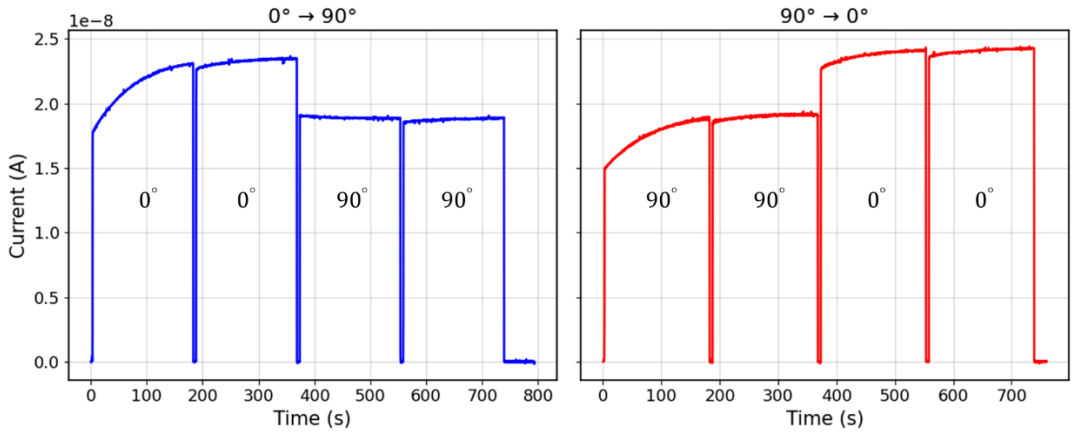

Figure 4.11. *Polarization dependent photocurrent response of the DASA–NWA device. Left: polarization switched from* 0° *to* 90°*; right: from* 90° *back to* 0°*. The photocurrent amplitude and rise behavior clearly vary with polarization, indicating an anisotropic light–matter coupling in the mixed DASA–NWA structure.*

As shown in **Figure 4.11**, the photocurrent amplitude strongly depends on the polarization direction. When the polarization angle is rotated from 0° to 90°, the peak current of the latter two pulses decreases noticeably, indicating that the device exhibits different absorption efficiencies under different polarization orientations. This result suggests that a certain degree of orientational coupling exists between the nanowire array and the DASA molecular layer, giving rise to directional dependence in light absorption and carrier generation.

However, the polarization switching experiments also reveal a clear residual coupling effect. When the polarization changes from 0° to 90°, the rise of the second pulse becomes slower, showing that the response is still affected by the illumination from the previous polarization state. Similarly, during the reverse switch from 90° back to 0°, the current does not fully return to its initial level. This implies that, although the system can distinguish different polarization states, the two polarization channels are not completely independent and show partial overlap.

Such partial coupling likely arises from two main factors:
(1) The molecular orientation is not fully aligned with the nanowire array. After drop-casting, DASA molecules may remain randomly distributed or only locally ordered, allowing light from any

polarization direction to excite a fraction of molecules;
(2) Optical reflections and scattering within the system. Some light may bypass the polarizer or be scattered by the sample surface, contributing additional photocurrent at all polarization angles.

In other words, the device exhibits clear anisotropic responses to polarization changes, yet these are not strictly independent channels but rather a pair of partially coupled polarization modes. This finding demonstrates that the mixed DASA–NWA system not only distinguishes between wavelengths (as shown in Section 4.4) but also responds to the vector nature of light, its polarization, thus expanding the dimensionality of optical information encoding.

From a broader perspective, this polarization dependence can be viewed as an additional degree of freedom in the system. By tuning the polarization direction of the incident light, it may be possible to switch between different signal channels or define logical states under the same wavelength. For instance, polarization angles of 0° and 90° could correspond to “writing Channel A” and “writing Channel B” respectively, realizing the wavelength-polarization combination coding to carry out a more complex modulation scheme. This feature has potential application value in future optical synapses and multi-dimensional photonic memory systems.

In summary, the polarization-dependent photocurrent of the DASA–NWA device confirms its sensitivity to the directionality of the light field. The different response amplitudes and kinetics observed at 0° and 90° polarizations reveal anisotropic coupling between the nanostructures and the molecular layers. Although partial overlap still exists between the polarization channels, this incomplete separation highlights the rich and multi-dimensional response mechanism of the system, laying the foundation for the future exploration of polarization-wavelength dual-control optical neural devices.

Chapter 5 – Conclusion and Outlook

5.1 Conclusions

This study systematically investigated the photo-response properties of two DASA molecules, D_R (AP-048) and D_G (AP-066), on the substrate of planar sapphire and silicon nanowire array (NWA). The objective is not only to achieve reversible optical modulation but also to understand the behavioral differences, interactions and influencing factors of the two dyes in the composite system. Several key conclusions were obtained through comprehensive measurements of absorption spectrum, bleaching recovery dynamics, multi-channel electrical responses and polarization dependence.

5.1.1 Photo-responsive characteristics of DASA molecules

D_R and D_G exhibit different photo-responsive behaviors, reflecting an intrinsic correlation between molecular structure and reaction dynamics. D_R molecule has stronger donor–acceptor coupling, faster reaction speed and greater bleaching amplitude under illumination, but it is also more likely to form irreversible species. In contrast, D_G has a more symmetric structure, weaker polarization, and a slower response speed, but demonstrates better stability. This difference highlights the direct influence of molecular electronic structure on photoreaction rates and suggests that the fast response of D_R may be suitable for real-time modulation, while the stability of D_G is conducive to long-term optical storage. In mixed films, both absorption bands of D_R and D_G were preserved, yet their bleaching processes were not entirely independent. A minor spectral overlap was observed, indicating partial coupling between the two chromophores. Such coupling likely arises from energy transfer, local optical field overlap, or inhomogeneous molecular distribution. Among all tested ratios, the mixture with D_R: $D_G \approx$ 1:20 showed the most balanced dual-band dynamics and the highest signal contrast. Repetitive illumination tests revealed a gradual reduction in reversible capacity due to partial irreversible bleaching or conformational rearrangement, while the overall spectral shape and peak positions remained unchanged. This indicates that the primary photochemical mechanism is still reversible, despite minor irreversible components.

5.1.2 DASA–NWA system and multichannel analysis

A dual-wavelength write–read protocol was implemented to define four communication channels. The results clearly distinguish between two response types: directly written channels (Channel 1 and 4) exhibited exponential decay corresponding to real molecular bleaching–recovery dynamics, while indirectly affected channels (Channel 2 and 3) showed approximately linear variations mainly arising from spectral overlap or optical noise. This comparison effectively distinguishes real molecular responses from optical crosstalk and provides a basis for kinetic modeling. The NWA structure significantly enhances light absorption and signal amplitude, making the exponential recovery behavior more evident, but also introduces partial crosstalk. Possible sources of crosstalk include limited spectral width of LEDs, energy transfer between dyes, or multiple scattering within the nanowire matrix. This study cannot completely separate the influence of these factors. Notably, the amplitude of the current of the write and read pulses exhibits a gradual increase over repeated cycles. The peak current increased by approximately 0.3–0.4%, indicating that a small number of

molecules remain permanently in the open or high conductivity state, thereby improving the overall conductivity. The predictable “stable degradation mode” reflects that the kinetic mechanism maintains unchanged, but the proportion of reversible molecules gradually decreases, which is a common feature in photochromic memory materials.

5.1.3 Polarization as an additional modulation channel

Polarization-dependent experiments demonstrate that the amplitude and response speed of photocurrent are sensitive to the polarization direction. When the polarization angle rotates from 0° to 90°, the current amplitude is significantly reduced; during the reverse switching, the signal is not fully recovered, implying that polarization can be used as an independent modulation parameter. Although the two polarization channels partially overlapped, the results confirm that polarization adds an extra degree of freedom for optical encoding. In other words, in addition to wavelength selectivity, polarization also offers an additional control dimension that may realize multi-dimensional optical memory and logic functionalities.

5.2 Outlook

This work is the first attempt to combine two DASA molecules in a nanowire array structure to achieve multi-wavelength and polarization-dependent optical responses. The whole research can be regarded as a gradual exploration process, starting with the optical physics of single dyes, and then gradually understanding their mixture behavior, optical dynamics and device-level characteristics. Although the conclusion is still preliminary, these experiments clarify the complexity of the system and point out the key direction for future research.

First, in terms of light source and spectral optimization, the current LED sources have relatively wide bandwidths, resulting in a nonnegligible spectral overlap between the red and green channel. Future work should adopt a narrower band and a more stable monochromatic or filtered light source to minimize crosstalk and achieve clearer bleaching dynamics. It is also necessary to determine the origin of the observed coupling, whether it comes from spectral overlap, energy transfer between dyes, or local scattering within the NWA. Combining tunable light sources with time-resolved spectroscopy would help to quantify these effects.

Second, for the study of polarization and structural anisotropy, this work only examined two extreme angles (0° and 90°). Future experiments should include higher-resolution angle scanning to build a full polarization-dependence profile and identify any periodic modulation pattern. Moreover, the application of an external electric field or the introduction of an alignment layer during film deposition may induce the orientation of some molecules, thereby enhancing polarization control and signal contrast.

Third, regarding experimental design and research strategy, this study prioritized understanding basic phenomena rather than achieving perfect control. Such an approach allows us to determine which factors are worth studying in depth and which can be temporarily neglected. Future experiments will follow this principle: maintaining flexibility to quickly capture trends, and gradually build quantitative datasets to improve the model. Some of the current interpretations may

later be revised or replaced after obtaining more accurate data, reflecting the natural development of experimental understanding.

Finally, concerning multi-dimensional optical memory and neuromorphic applications, the DASA–NWA platform exhibits controllability in both wavelength and polarization dimensions, so that it can be composited in a single structure. When combined with spatial resolution or array-based design, this method could be developed into multi-pixel, multi-channel optical memory devices. The integration of wavelength, polarization and temporal modulation may realize the demonstration of complex optical synapse behaviors and programmable light-driven logic functions.

In summary, this study provides new experimental insights into the optical behavior of DASA molecules in the nanostructured environment. Although the current results are not final, the analysis of channel behavior, mixing ratios and polarization response have deepened our understanding of the system. Future work will continue to be carried out in these directions, combining refined experiments with modeling to further clarify the potential of DASA–NWA system for multi-dimensional optical information memory and optoelectronic functional devices.

Reference list

[1]. Sebastian, A., Le Gallo, M., Khaddam-Aljameh, R., & Eleftheriou, E. (2020). Memory devices and applications for in-memory computing. *Nature nanotechnology*, *15*(7), 529-544.

[2]. Mutlu, O., Ghose, S., Gómez-Luna, J., & Ausavarungnirun, R. (2019). Processing data where it makes sense: Enabling in-memory computation. *Microprocessors and Microsystems*, *67*, 28-41.

[3]. Azevedo, F. A., Carvalho, L. R., Grinberg, L. T., Farfel, J. M., Ferretti, R. E., Leite, R. E., ... & Herculano-Houzel, S. (2009). Equal numbers of neuronal and nonneuronal cells make the human brain an isometrically scaled-up primate brain. *Journal of Comparative Neurology*, *513*(5), 532-541.

[4]. Chen, X., Chen, B., Zhao, P., Roy, V. A., Han, S. T., & Zhou, Y. (2023). Nanowire-based synaptic devices for neuromorphic computing. *Materials Futures*, *2*(2), 023501.

[5]. Ohno, T., Hasegawa, T., Tsuruoka, T., Terabe, K., Gimzewski, J. K., & Aono, M. (2011). Short-term plasticity and long-term potentiation mimicked in single inorganic synapses. *Nature materials*, *10*(8), 591-595.

[6]. Zhang, K., Xue, Q., Zhou, C., Mo, W., Chen, C. C., Li, M., & Hang, T. (2022). Biopolymer based artificial synapses enable linear conductance tuning and low-power for neuromorphic computing. *Nanoscale*, *14*(35), 12898-12908.

[7]. Furber, S. (2016). Large-scale neuromorphic computing systems. *Journal of neural engineering*, *13*(5), 051001.

[8]. Chiang, A. S., Lin, C. Y., Chuang, C. C., Chang, H. M., Hsieh, C. H., Yeh, C. W., ... & Hwang, J. K. (2011). Three-dimensional reconstruction of brain-wide wiring networks in Drosophila at single-cell resolution. *Current biology*, *21*(1), 1-11.

[9]. Giurfa, M. (2013). Cognition with few neurons: higher-order learning in insects. *Trends in neurosciences*, *36*(5), 285-294.

[10]. Wehner, R. (2003). Desert ant navigation: how miniature brains solve complex tasks. *Journal of Comparative Physiology A*, *189*(8), 579-588.

[11]. Menzel, R. (2012). The honeybee as a model for understanding the basis of cognition. *Nature Reviews Neuroscience*, *13*(11), 758-768.

[12]. Pfeiffer, K., & Homberg, U. (2014). Organization and functional roles of the central complex in the insect brain. *Annual review of entomology*, *59*(1), 165-184.

[13]. Collett, M., Chittka, L., & Collett, T. S. (2013). Spatial memory in insect navigation. *Current Biology*, *23*(17), R789-R800.

[14]. Zeil, J. (2012). Visual homing: an insect perspective. *Current opinion in neurobiology*, *22*(2), 285-293.

[15]. Heinze, S. (2017). Unraveling the neural basis of insect navigation. *Current opinion in insect science*, *24*, 58-67.

[16]. Degen, J., Kirbach, A., Reiter, L., Lehmann, K., Norton, P., Storms, M., ... & Menzel, R. (2016). Honeybees learn landscape features during exploratory orientation flights. *Current Biology*, *26*(20), 2800-2804.

[17]. Evangelista, C., Kraft, P., Dacke, M., Labhart, T., & Srinivasan, M. V. (2014). Honeybee navigation: critically examining the role of the polarization compass. *Philosophical Transactions of the Royal Society B: Biological Sciences*, *369*(1636), 20130037.

[18]. Honkanen, A., Adden, A., da Silva Freitas, J., & Heinze, S. (2019). The insect central complex and the neural basis of navigational strategies. *Journal of Experimental Biology*, *222*(Suppl_1), jeb188854.

[19]. Chaurasiya, R., Shih, L. C., Chen, K. T., & Chen, J. S. (2023). Emerging higher-order memristors for bio-realistic neuromorphic computing: A review. *Materials Today*, *68*, 356-376.

[20]. Mayr, C., Partzsch, J., Noack, M., Hänzsche, S., Scholze, S., Höppner, S., ... & Schüffny, R. (2015). A biological-realtime neuromorphic system in 28 nm CMOS using low-leakage switched capacitor circuits. *IEEE transactions on biomedical circuits and systems*, *10*(1), 243-254.

[21]. Muñoz-Martin, I., Bianchi, S., Hashemkhani, S., Pedretti, G., Melnic, O., & Ielmini, D. (2021). A brain-inspired homeostatic neuron based on phase-change memories for efficient neuromorphic computing. *Frontiers in Neuroscience*, *15*, 709053.

[22]. Yan, R., Gargas, D., & Yang, P. (2009). Nanowire photonics. *Nature photonics*, *3*(10), 569-576.

[23]. Li, Z., He, Z., Xi, C., Zhang, F., Huang, L., Yu, Y., ... & Fu, L. (2023). Review on III–V semiconductor nanowire array infrared photodetectors. *Advanced Materials Technologies*, *8*(13), 2202126.

[24]. Shastri, B. J., Tait, A. N., Ferreira de Lima, T., Pernice, W. H., Bhaskaran, H., Wright, C. D., & Prucnal, P. R. (2021). Photonics for artificial intelligence and neuromorphic computing. Nature Photonics, 15(2), 102-114.

[25]. Flodgren, V., Das, A., Sestoft, J. E., Alcer, D., Jensen, T. K., Jeddi, H., ... & Mikkelsen, A. (2025). Direct on-chip optical communication between nano optoelectronic devices. ACS photonics, 12(2), 655-665.

[26]. Hemmer, James R., et al. "Tunable visible and near infrared photoswitches." *Journal of the American Chemical Society* 138.42 (2016): 13960-13966.

[27]. Philip, Abbey M., Marie E. Krogh, and Bo W. Laursen. "Robust Red-Absorbing Donor-Acceptor Stenhouse Adduct Photoswitches." *Chemistry–A European Journal* 30.30 (2024): e202400621.

[28]. Stricker, F., Sanchez, D. M., Raucci, U., Dolinski, N. D., Zayas, M. S., Meisner, J., ... & Read de Alaniz, J. (2022). A multi-stage single photochrome system for controlled photoswitching responses. Nature Chemistry, 14(8), 942-948.

[29]. Alcer, D., Zaiats, N., Jensen, T. K., Philip, A. M., Gkanias, E., Ceberg, N., ... & Mikkelsen, A. (2025). Integrating molecular photoswitch memory with nanoscale optoelectronics for

neuromorphic computing. Communications Materials, 6(1), 11.

[30]. Jang, H., Ju, S., Lee, S., Choi, J., Byun, U., Min, K., ... & Kim, S. (2025). Recent Advances in Optoelectronic Synaptic Devices for Neuromorphic Computing. Biomimetics, 10(9), 584.

[31]. Zhou, M., Zhao, Y., Gu, X., Zhang, Q., Zhang, J., Jiang, M., & Lu, S. (2023). Light-stimulated low-power artificial synapse based on a single GaN nanowire for neuromorphic computing. Photonics Research, 11(10), 1667-1677.

[32]. Zhou, M., Zhao, Y., Gu, X., Zhang, Q., Zhang, J., Jiang, M., & Lu, S. (2023). Realize low-power artificial photonic synapse based on (Al, Ga) N nanowire/graphene heterojunction for neuromorphic computing. APL Photonics, 8(7).

[33]. Li, G. (2023). Artificial optical synaptic devices with ultra-low power consumption. Light: Science & Applications, 12(1), 24.

[34]. Lan, L., Huang, B., Li, Y., Wang, C., Pan, J., Huang, J., ... & Cao, Y. (2025). Stretchable optoelectronic synapses with ultraviolet to near-infrared perception for retina-inspired computing and vision-adaptive sensing. npj Flexible Electronics, 9(1), 16.

[35]. He, M., & Tang, X. (2025, April). Recent Progress in Organic Optoelectronic Synaptic Devices. In Photonics (Vol. 12, No. 5, p. 435). MDPI.

[36]. Hu, G., An, H., Xi, J., Lu, J., Hua, Q., & Peng, Z. (2021). A ZnO micro/nanowire-based photonic synapse with piezo-phototronic modulation. Nano Energy, 89, 106282.

[37]. Sze, S. M., Li, Y., & Ng, K. K. (2021). *Physics of semiconductor devices*. John wiley & sons.

[38]. Hu, C. (2009). PN and metal-semiconductor junctions. *UC, Berkeley, EE Class Note*, 89-156.

[39]. Shockley, W. (1949). The Theory of p-n Junctions in Semiconductors and p-n Junction Transistors. *Bell system technical journal*, *28*(3), 435-489.

[40]. Zhu, Y., Raj, V., Li, Z., Tan, H. H., Jagadish, C., & Fu, L. (2021). Self-powered InP nanowire photodetector for single-photon level detection at room temperature. *Advanced Materials*, *33*(49), 2105729.

[41]. Fischer, I. A., Augel, L., Jitpakdeebodin, S., Franz, N., Fleischer, S., & Schulze, J. (2015, June). Plasmonics-integrated Ge PIN-photodetectors: efficiency enhancement by Al nanoantennas and plasmon detection. In *International Conference on Optics and Photonics 2015* (Vol. 9654, pp. 22-27). SPIE.

[42]. Anttu, N. (2023). Absorption of light in vertical III-V semiconductor nanowires for solar cell and photodetector applications. *Crystals*, *13*(9), 1292.

[43]. Halpern, E., Elias, G., Kretinin, A. V., Shtrikman, H., & Rosenwaks, Y. (2012). Direct measurement of surface states density and energy distribution in individual InAs nanowires. *Applied Physics Letters*, *100*(26).

[44]. Han, Y., Fu, M., Tang, Z., Zheng, X., Ji, X., Wang, X., ... & Chen, Q. (2017). Switching from negative to positive photoconductivity toward intrinsic photoelectric response in InAs nanowire. *ACS applied materials & interfaces*, *9*(3), 2867-2874.

[45]. Mauthe, S., Baumgartner, Y., Sousa, M., Ding, Q., Rossell, M. D., Schenk, A., ... & Moselund,

K. E. (2020). High-speed III-V nanowire photodetector monolithically integrated on Si. *Nature communications*, *11*(1), 4565.

[46]. Dayeh, S. A., Aplin, D. P., Zhou, X., Yu, P. K., Yu, E. T., & Wang, D. (2007). High electron mobility InAs nanowire field-effect transistors. *small*, *3*(2), 326-332.

[47]. Ford, A. C., Ho, J. C., Chueh, Y. L., Tseng, Y. C., Fan, Z., Guo, J., ... & Javey, A. (2009). Diameter-dependent electron mobility of InAs nanowires. *Nano Letters*, *9*(1), 360-365.

[48]. Shin, J., & Yoo, H. (2023). Photogating effect-driven photodetectors and their emerging applications. *Nanomaterials*, *13*(5), 882.

[49]. Karmakar, A., Mileo, P. G., Bok, I., Peh, S. B., Zhang, J., Yuan, H., ... & Zhao, D. (2020). Thermo-responsive MOF/polymer composites for temperature-mediated water capture and release. *Angewandte Chemie International Edition*, *59*(27), 11003-11009.

[50]. Zhu, J., Lin, H., Kim, Y., Yang, M., Skakuj, K., Du, J. S., ... & Mirkin, C. A. (2020). Light-Responsive Colloidal Crystals Engineered with DNA. *Advanced Materials*, *32*(8), 1906600.

[51]. Gamerith, C., Luschnig, D., Ortner, A., Pietrzik, N., Guse, J. H., Burnet, M., ... & Gübitz, G. M. (2019). pH-responsive materials for optical monitoring of wound status. *Sensors and Actuators B: Chemical*, *301*, 126966.

[52]. Gomes, R. F., Coelho, J. A., & Afonso, C. A. (2018). Synthesis and applications of Stenhouse salts and derivatives. *Chemistry–A European Journal*, *24*(37), 9170-9186.

[53]. Balamurugan, A., & Lee, H. I. (2016). A visible light responsive on–off polymeric photoswitch for the colorimetric detection of nerve agent mimics in solution and in the vapor phase. *Macromolecules*, *49*(7), 2568-2574.

[54]. Helmy, S., Oh, S., Leibfarth, F. A., Hawker, C. J., & Read de Alaniz, J. (2014). Design and synthesis of donor–acceptor stenhouse adducts: a visible light photoswitch derived from furfural. *The Journal of organic chemistry*, *79*(23), 11316-11329.

[55]. Helmy, S., Leibfarth, F. A., Oh, S., Poelma, J. E., Hawker, C. J., & Read de Alaniz, J. (2014). Photoswitching using visible light: a new class of organic photochromic molecules. *Journal of the American Chemical Society*, *136*(23), 8169-8172.

[56]. Di Donato, M., Lerch, M. M., Lapini, A., Laurent, A. D., Iagatti, A., Bussotti, L., ... & Feringa, B. L. (2017). Shedding light on the photoisomerization pathway of donor–acceptor stenhouse adducts. *Journal of the American Chemical Society*, *139*(44), 15596-15599.

[57]. Jia, S., Tan, A., Hawley, A., Graham, B., & Boyd, B. J. (2019). Visible light-triggered cargo release from donor acceptor Stenhouse adduct (DASA)-doped lyotropic liquid crystalline nanoparticles. *Journal of colloid and interface science*, *548*, 151-159.

[58]. Sorour, M. I., Kistler, K. A., Marcus, A. H., & Matsika, S. (2021). Accurate modeling of excitonic coupling in cyanine dye Cy3. *The Journal of Physical Chemistry A*, *125*(36), 7852-7866.

[59]. Valeur, B., & Berberan-Santos, M. N. (2013). *Molecular fluorescence: principles and applications*. John Wiley & Sons.

[60]. Chueh, C. C., Li, C. Z., & Jen, A. K. Y. (2015). Recent progress and perspective in solution-processed Interfacial materials for efficient and stable polymer and organometal perovskite solar cells. *Energy & Environmental Science*, *8*(4), 1160-1189.

[61]. Scherf, U., & List, E. J. (2002). Semiconducting polyfluorenes—towards reliable structure–property relationships. *Advanced Materials*, *14*(7), 477-487.

[62]. Citri, A., & Malenka, R. C. (2008). Synaptic plasticity: multiple forms, functions, and mechanisms. *Neuropsychopharmacology*, *33*(1), 18-41.

[63]. Malenka, R. C., & Bear, M. F. (2004). LTP and LTD: an embarrassment of riches. *Neuron*, *44*(1), 5-21.

[64]. Lakowicz, J. R. (Ed.). (2006). *Principles of fluorescence spectroscopy*. Boston, MA: springer US.

[65]. Heyne, B. (2016). Self-assembly of organic dyes in supramolecular aggregates. *Photochemical & Photobiological Sciences*, *15*(9), 1103-1114.

Appendix

A Table: Model Parameters of Photosensitive PFET

Parameter	Symbol	Typical Value	Unit	Physical Meaning
Gate Voltage	V_g	$-2 \sim 5$	V	External voltage applied to the gate electrode
Threshold Voltage (Dark)	$V_{th,dark}$	1.7	V	Threshold voltage of the channel in dark conditions
Threshold Voltage (Illuminated)	$V_{th,light}$	1.3	V	Threshold voltage of the channel under illumination
Threshold Shift	ΔV_{th}	0.4	V	Shift in threshold voltage induced by illumination
Transconductance Coefficient (Dark)	k_{dark}	1.0×10^{-6}	A/V^2	Channel carrier mobility in dark conditions
Transconductance Coefficient (Illuminated)	k_{light}	1.25×10^{-6}	A/V^2	Channel carrier mobility under illumination
Gate Oxide Thickness	t_{ox}	15	nm	Thickness of HfO_2 layer
Nanowire Diameter	D_{NW}	60	nm	Diameter of InAs nanowire
Channel Length	L_{ch}	2.0	μm	Distance between source and drain electrodes
Optical Power Density	P_{opt}	1.0	mW/cm^2	Intensity of incident light

B Illumination Optimization Tests

This appendix introduces the parameter scanning experiments to determine the optimal illumination intensities for the Read and Write pulses.

All measurements were performed on the same DASA–NWA sample to test the responses of LED-G (corresponding to AP-066) and LED-R (corresponding to AP-048) at different power levels and pulse intervals.

B.1 Write Pulse Optimization

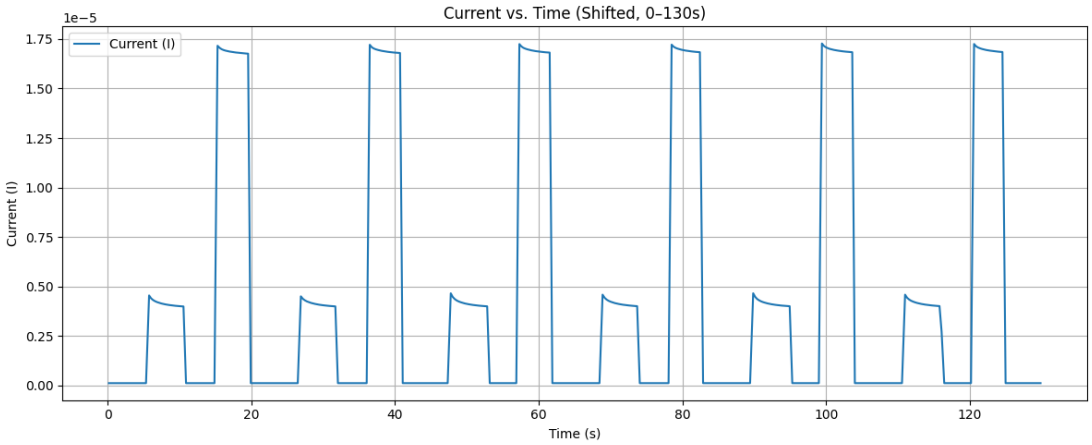

Figure B1. Raw current trace of alternating LED-G (Write-G) and LED-R (Write-R) pulses at Power 3000. Due to the contribution of solar cells in the nanowire array, pulses 1 and 2 both show strong overshoot and bending. High intensities ($\geq 10\ mW\ cm^{-2}$) saturate the photo-response and cover up the dye dynamics. Lowering the illumination reduces this effect and reveals the kinetics of molecular bleaching.

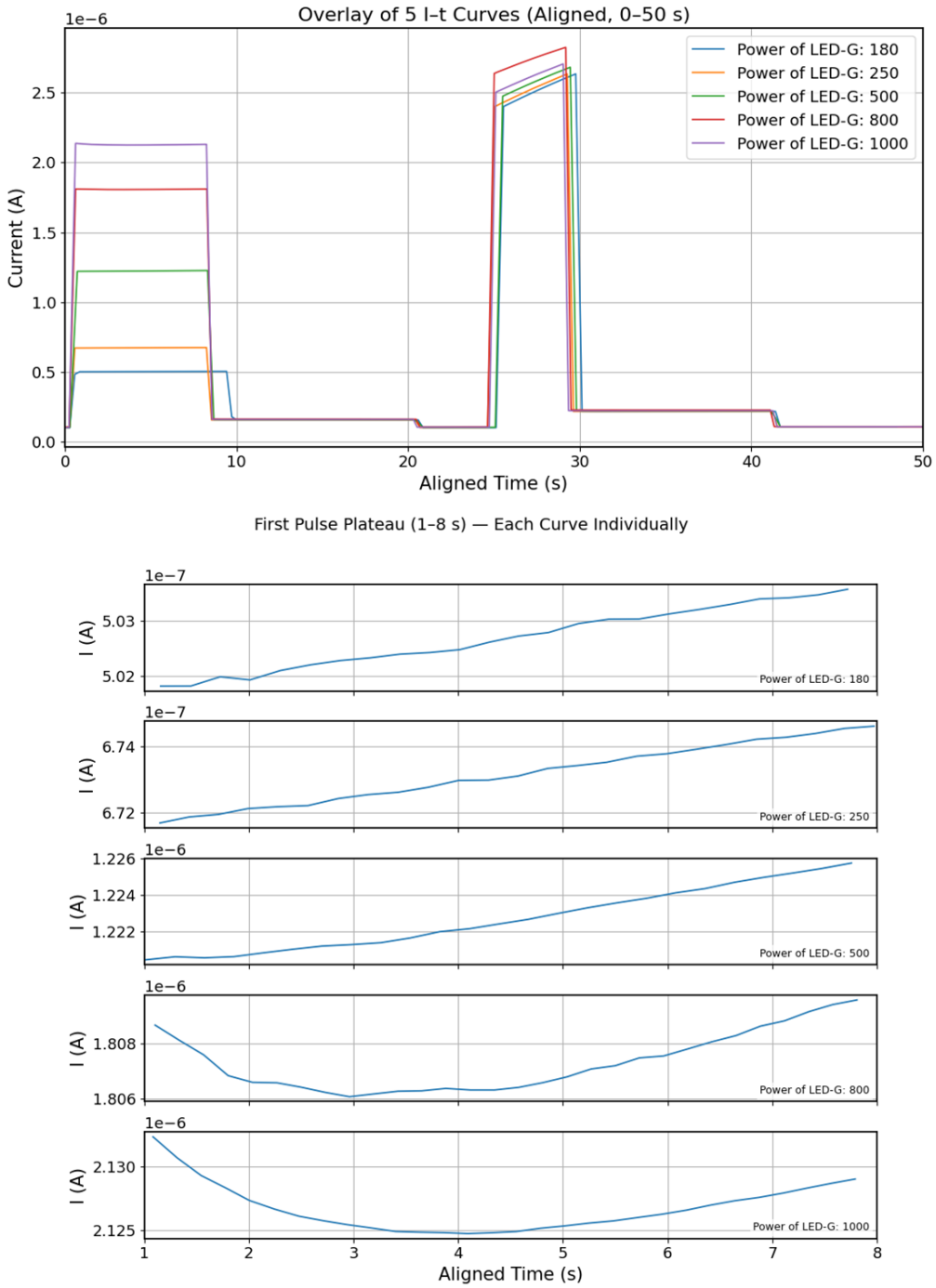

Figure B2. Overlay of five I–t curves (Power 180 – 1000) shows the bleaching behavior of dyes. D_G exhibits strong absorption and clear photobleaching even at low power, while D_R has low sensitivity. When the power exceeds 500, the signal shows a downward trend, indicating that the nanowire photocurrent dominates. Therefore, Power 500 (≈ 0.3 mW cm^{-2}) was selected for both Write-G and Write-R as the optimal balance between bleaching efficiency and molecular selectivity.

B.2 Read Pulse Optimization – LED-G

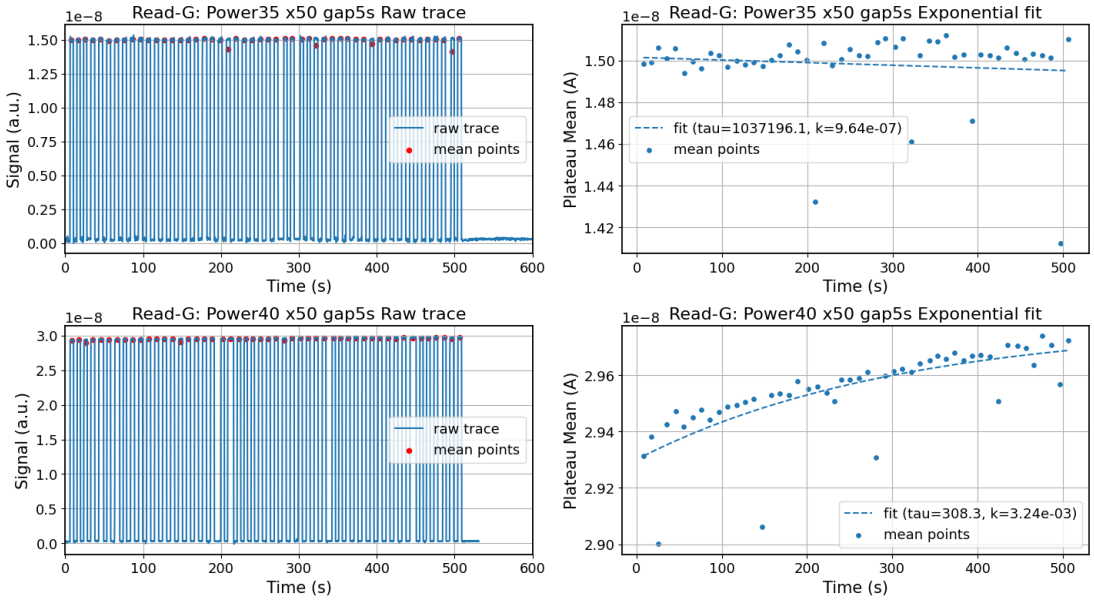

Figure B3. Comparison of Read-G responses at Power 35 and Power 40. When the Power is 35, the plateau currents remain stable; at Power 40, a gradual increase appears, implying partial bleaching. Hence, select Power 35 as the safe upper limit for Read-G measurement.

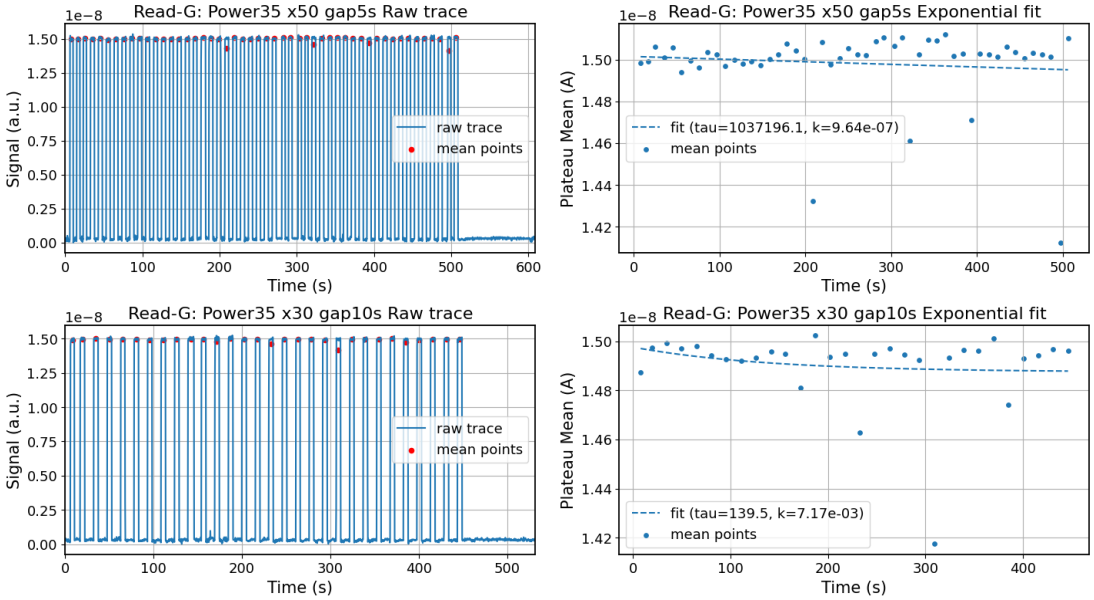

Figure B4. The effect of pulse interval (5 seconds vs 10 seconds) on Read-G response at Power 35. No significant difference was observed, which confirmed that the time interval between Read pulses is negligible.

B.3 Read Pulse Optimization – LED-R

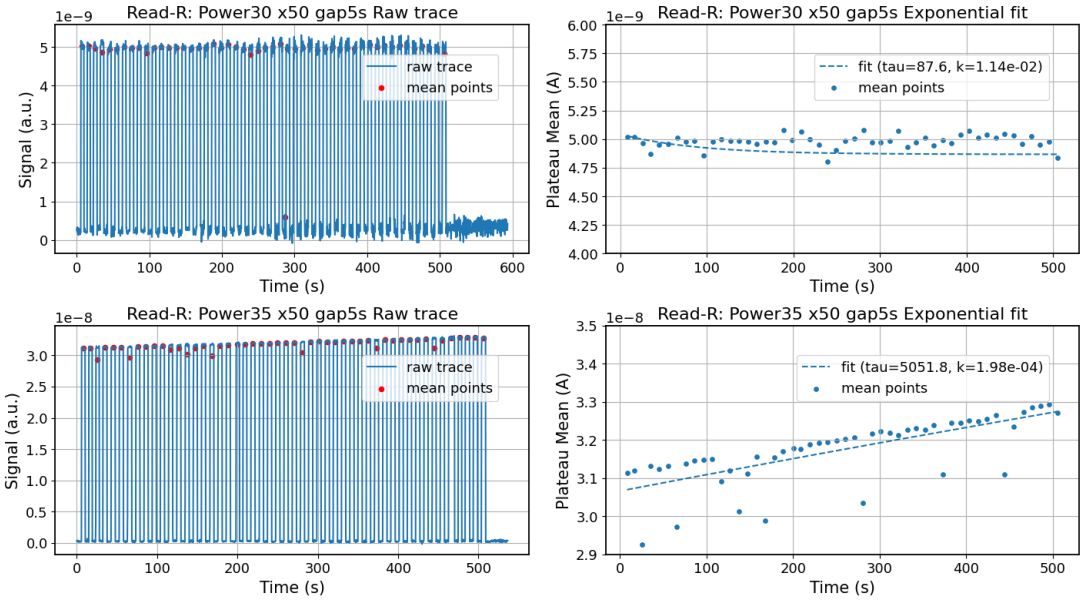

Figure B5. Comparison of Read-R responses at Power 30 and 35. At Power 30, the signal remains stable; at Power 35, the plateau period increases over time, indicating unnecessary bleaching. Thus, the Read-R selection Power is 30.

B.4 Cross-Channel Verification

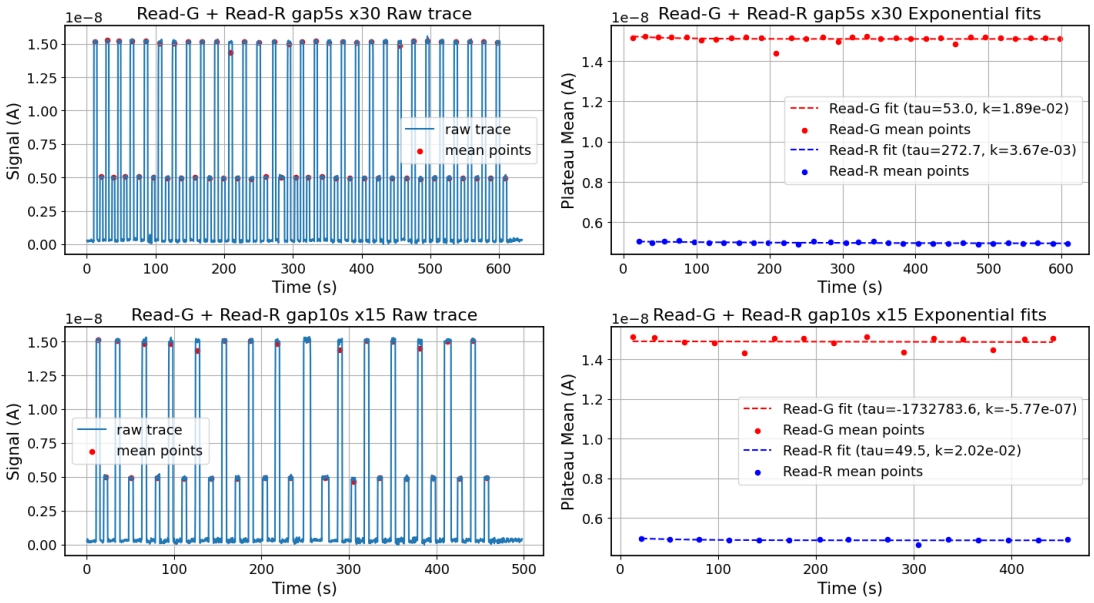

Figure B6. Sequential Read-G → Read-R tests at different pulse gaps (5 seconds × 30 and 20 seconds × 15). In both sets of data, Read-G and Read-R show stable plateau levels, indicating that one Read channel does not affect the other.

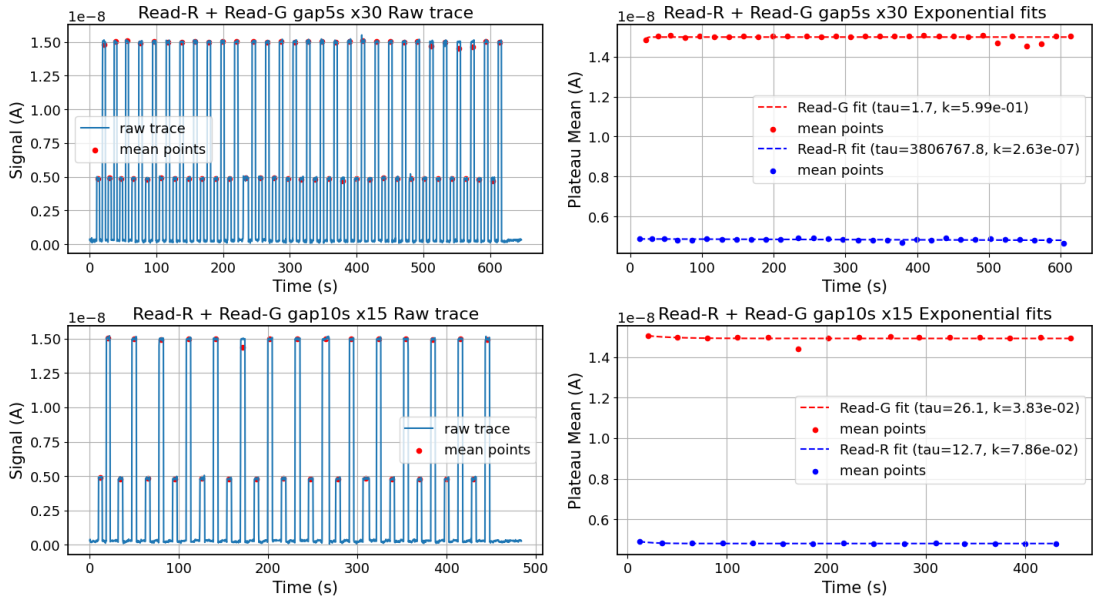

Figure B7. Reversed Read-R → Read-G tests confirms the same conclusion that there is no significant crosstalk between the two wavelengths.

B.5 Summary of Optimized Parameters

Parameter	Symbol	Optimal Power Setting	Estimated Intensity ($mW\ cm^{-2}$)	Interval (s)	Behavior
Write (G)	LED-G	500	~0.30	—	Complete bleaching, no solar-cell dominance
Write (R)	LED-R	500	~0.30	—	Moderate bleaching, stable plateau
Read (G)	LED-G	35	~0.02	5 s (between R and R)	No bleaching, stable output
Read (R)	LED-R	30	~0.015	5 s (between R and R)	No bleaching, stable output
Read-group interval	—	—	—	10 s (between R-G/R groups)	No accumulation effect

B.6 Discussion

These results indicate that light intensity plays a crucial balance between the molecular bleaching kinetics and the photovoltage effects of nanowire arrays. When the illumination is too strong, the signal trend changes from increasing to decreasing, suggesting that carrier generation is dominated by the photovoltaic response of nanowires, not the molecular bleaching process. Moderate reduction of light intensity can not only reveal the inherent dye response, but also significantly reduce the accumulation of irreversible bleaching.

This observation is consistent with previous studies, which suggest that for DASA system, investigating the kinetics of about 50% bleaching can provide more meaningful physical insights than pursuing full bleaching. At this intermediate state, the contrast between absorption states is still visible and the reversibility is maintained.

Therefore, the illumination scheme used in this study (Write $\approx$ $0.3\ mW\ cm^{-2}$, Read $\approx$ $0.02 - 0.03\ mW\ cm^{-2}$) achieves an optimal balance between bleaching efficiency, signal-to-noise ratio and sample longevity.

B.7 Description of Figures B1–B7

Figures B1–B7 show the experimental results of the illumination optimization processin turn, including power-dependent response curves, pulse interval tests, and cross-channel validation for both LED-G and LED-R. Each diagram corresponds to one step to determine the final working parameters summarized in Section 4.4.

Figure ID	Summary of Content
B1	Write-pulse overshoot and solar-cell dominance at high power (3000)
B2	LED-G and LED-R power dependence (180–1000); optimal = 500
B3	Read-G Power 35 vs 40 comparison
B4	Read-G pulse interval 5 s vs 10 s
B5	Read-R Power 30 vs 35 comparison
B6	Read-G→Read-R sequence (5 s/20 s intervals)
B7	Read-R→Read-G sequence (5 s/20 s intervals)